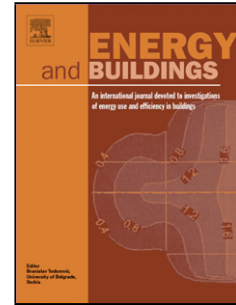


Accepted Manuscript

Title: Modeling of Double Skin Façades Integrating Photovoltaic Panels and automated roller shades: Analysis of the Thermal and Electrical Performance

Authors: Z. Ioannidis, A. Buonomano, A.K. Athienitis, T. Stathopoulos



PII: S0378-7788(17)31785-1
DOI: <http://dx.doi.org/10.1016/j.enbuild.2017.08.046>
Reference: ENB 7875

To appear in: *ENB*

Received date: 24-5-2017
Revised date: 7-8-2017
Accepted date: 17-8-2017

Please cite this article as: Z.Ioannidis, A.Buonomano, A.K.Athienitis, T.Stathopoulos, Modeling of Double Skin Façades Integrating Photovoltaic Panels and automated roller shades: Analysis of the Thermal and Electrical Performance, Energy and Buildings <http://dx.doi.org/10.1016/j.enbuild.2017.08.046>

This is a PDF file of an unedited manuscript that has been accepted for publication. As a service to our customers we are providing this early version of the manuscript. The manuscript will undergo copyediting, typesetting, and review of the resulting proof before it is published in its final form. Please note that during the production process errors may be discovered which could affect the content, and all legal disclaimers that apply to the journal pertain.

Modeling of Double Skin Façades Integrating Photovoltaic Panels and automated roller shades: Analysis of the Thermal and Electrical Performance

Z. Ioannidis^{*1}, A. Buonomano^{1,2}, A.K. Athienitis¹, T. Stathopoulos¹

¹Centre for Zero Energy Building Studies, Department of Building, Civil and Environmental Engineering, Concordia University, 1455 de Maisonneuve Blvd. W., Montreal, H3G 1M8 QC, Canada

²Department of Industrial Engineering, University of Naples Federico II, P.le Tecchio, 80, 80125 Naples, Italy

*Corresponding author e-mail: z_ioann@encs.concordia.ca

Abstract

A numerical model is developed for simulating a single or multi-story Double Skin Façade integrating Photovoltaics (DSF-PV). The DSF-PV can co-generate solar electricity and heat while it also allows daylight to be transmitted to the interior space. The buoyancy-driven air flow inside the cavity may be assisted by a fan to cool down the photovoltaics while providing natural or hybrid ventilation to adjacent zones. Automated roller shades are also implemented in the model and help regulate heating and cooling loads but also control the daylight levels in the indoor space. A parametric analysis for different control strategies for the airflow within the cavity and the roller shading devices is performed with the purpose to apply the proposed methodology to minimize the heating and cooling demand of the DSF-PV system. In addition, a parametric analysis for different adjacent zones floor areas is performed. The simulations show that a DSF-PV system can supply approximately 120kWh/façade area/year covering the yearly electricity demand of the adjacent office if the floor area is approximately less than 3 times larger than the floor area.

Keywords: Double Skin Façade; BIPV; BIPV/T; Photovoltaics; multi-story; energy consumption.

Nomenclature

A	Heat exchange surface area (m ²)	<i>g</i>	Glazing
C	Thermal capacitance (J/K)	<i>in</i>	Indoor air
Cd	Discharge coefficient for the orifice (-)	<i>ins</i>	Insulation
Cf	Flow Coefficient (m ^{2.5} kg ^{-0.5})	<i>int</i>	Interior
<i>c_p</i>	Specific heat capacity (kJ/kgK)	<i>mech</i>	Mechanical
Cp	Pressure coefficient (-)	<i>n</i>	Node of the thermal network
d	Profile angle (°)	<i>nat</i>	Natural
D	Hydraulic diameter (m)	<i>OPV</i>	Opaque photovoltaic
E	Total emissive power (W/m ²)	<i>out</i>	Ambient
f	Surface view factor (-)	<i>ov</i>	Overhang

F	View factors (-)	PV	Photovoltaic
H	Height (m)	rad	Radiation
h	Heat transfer coefficient (W/m ² K)	rol	Roller blind
I	Solar radiation flux (W/m ²)	sh	Shade/Shading
J	Radiosity (W/m ²)	sky	Sky vault
K	Thermal conductivity (W/mK)	sp	Set-point
L	Room length (m)	spd	Spandrel
m	Mass flow rate (kg/s)	stc	Standard test conditions
Nu	Nusselt number (-)	STPV	Semi-transparent photovoltaic
PV	Photovoltaic	th	Thermal
Q̇	Thermal load (W)	uspd	Upper spandrel
R	Thermal resistance (K/W)	w	Wind
Re	Reynolds number (-)	wd	Window
Rs	Roller position (%)	wg	Referred to water vapour gain
S	Solar energy (W)	wi	Interior wall section
Ŝ	Interreflected Solar Radiation (W)	wl	Wall
T	Temperature (K)	wo	Exterior wall section
t	Time (s)	z	Building adjacent zone number
V	Velocity (m/s)		
W	Room width (m)		
y	Distance (m)		
<i>Superscript/Subscripts</i>			
air	Air of the cavity		
ca	Cavity		
db	Dry bulb air		
dir	Direct		
el	Electricity		
ext	Exterior		
f	Façade		
fl	Floor		
mlt	Multiple interreflections		
<i>Greeks letters</i>			
		α	Absorption factor (-)
		α_s	Surface azimuth (°)
		α_s	Solar altitude (°)
		ε	Emissivity (-)
		η	Photovoltaic efficiency (-)
		θ	Wind direction (°)
		μ	Dynamic viscosity (Ns/m ²)
		ρ	Air density (kg/m ³)
		ρ	Reflectivity (-)
		σ	Stefan-Boltzmann constant (5.67 10 ⁻⁸ W/m ² K ⁴)
<i>Abbreviations</i>			
AH	Auxiliary Heater	EER	Energy Efficiency Ratio
BIPV/T	Building Integrated Photovoltaics Thermal	HP	Heat Pump
CFD	Computational Fluid Dynamics	NZEB	Net Zero Energy Building
CH	Chiller	PLR	Part Load Ratio
COP	Coefficient Of Performance	PV/T	Photovoltaic Thermal
DSF	Double Skin Façade	SHCG	Solar Heat Gain Coefficient
DSF-PV	Double Skin Façade integrating Photovoltaics	STPV	Semi -Transparent Photovoltaic

1 Introduction

In the recent years, the growing concerns about the energy consumptions in buildings has led the research community toward the development of sustainable building energy policies (e.g. EPBD, etc.) and the promotion of the next generation buildings, such as net zero-energy building (NZEB) [1]. In order to reach the NZEB goal, the use of innovative building concepts and materials, along with the implementation of energy efficient and renewable technologies are becoming more and more relevant [2]. Energy efficiency technologies are required to effectively exploit renewable energy sources and to also avoid the mismatch between the produced renewable energy and the building load profiles, especially in the case of solar energy [3], [4]. To this twofold aim, advanced Double Skin Façades (DSFs) were identified as one of the most promising responsive building elements (i.e. IEA–ECBCS Annex 44, [5]) and have gained an increasing attention [6]. DSFs became an important architectural building element due to their high potential to provide energy, comfort, aesthetic and structural advantages, as well as to provide space for integrated PV panels [7]. Therefore, DSFs are one of the buildings key new features, especially in case of high-rise buildings which can efficiently take advantage of their wide exposed envelope area for the exploitation of the solar energy.

A DSF normally consists of an exterior and an interior skin separated by a ventilated air cavity used as air channel (Figure 1) [8]. This cavity is considered as a buffer zone and it is located between the exterior skin and the insulated interior one of a newly built or a renovated building. In the case of retrofits, the addition of an external layer may also be a cost effective measure to improve the energy efficiency of the building as it can be used to integrate photovoltaics [7]. The cavity of the DSF can also create a microclimate around the building, adding climate resilience to it and making it possible to adapt to weather changes. Also the temperature differences inside the cavity can facilitate natural ventilation or hybrid ventilation [9] and it can be used for heat recovery purposes, reducing in this way the heating or cooling loads of the building. The addition of an external layer can improve acoustic comfort and protect the building from wind or rain penetration [9]–[11]. In particular, to avoid rain penetration, one simple type of DSF (i.e. rain screen wall) applies pressure equalization for which airflow and pressures inside the cavity are important [12]. DSFs also provide the opportunity to use operable windows and at the same time extend the usable indoor space area near the window. The integration of photovoltaics (PVs) on the exterior skin, along with the implementation of controlled shading devices within the cavity of a DSF, gives the opportunity to design an energy positive DSF façade. This can be achieved by the generation of electricity through integrated PVs, the control of solar heat gains and by the extraction of heat from the PVs and the shading device by the air flowing within the cavity.

In order to improve the energy and comfort performance of DSFs, diverse effective system geometries and airflow concepts [8] as well as novel integrated designs [13] have been recently investigated. The available studies on the DSF performance show that façade design, building and site parameters are identified to be the most important parameters influencing the performance of the DSF [14]. Simulations of a naturally ventilated multi-story DSF were held investigating the impact that the orientation of the building, the wind direction and the different strategies have on the performance of a DSF [15]–[17]. The adoption of integrated thermal mass aimed to improve the energy performance of DSFs was also studied [18], [19]. DSF also has showed a significant potential for daylight control and energy savings through the use of shading devices like louvers or blinds [20]–[23]. Nevertheless, the

available literature shows that the research was mainly focused on the ventilation of the DSF, whereas wind effects, daylighting and integration of photovoltaics have not been extensively studied yet [10].

The majority of the studies available in the literature that analyze the airflow inside the cavity use computational fluid dynamics (CFD) analysis. CFD tools are used to predict the airflow and the temperature inside the cavity of the DSF [24] and to simulate the free and forced convection between the air and the skins of the DSF [25]. CFD simulations are also held in order to characterize the airflow around the shading devices implemented within the cavity of the DSF [26]. The most studied shading device implemented in a DSF is venetian blind, and several analyses were carried out to assess its impact on the airflow and heat transfer [27]–[29].

The heat transfer phenomena in an airflow window with building integrated PV/T [30], and the optimization of the performance of a DSF with integrated opaque photovoltaics [31], were extensively studied. Whilst electrical, thermal, and visual performances of a semitransparent thin-film PV facade were studied by several authors [32]–[35], DSF with integrated semi-transparent photovoltaics were only recently analyzed [36], [37]. The annual overall energy performance, energy-saving and daylighting potential, of a ventilated DSF were numerically simulated by means of Energy Plus. Simulations and sensitivity analyses about the air cavity width and ventilation modes were carried out for a cool-summer Mediterranean climate zone [38].

Computer based numerical simulations have been extensively used with the aim to predict the thermal performance of DSF under different environmental conditions. Diverse numerical methods have been used, reviewed and discussed [39]. The analysis of the state of the art shows that there are no standard procedures, adopted by researchers, for reporting and comparing the obtained simulation results, thus further research is required with the purpose to compare all models with the same experimental test. In addition, the produced studies and models are mainly focused on the energy performance and thermal behavior of the DSF itself, whilst there is a need to develop energy simulation models capable to assess the active and passive effects of the DSF on a whole building level [14], [39].

In order to assess the effects of DSF on the building energy consumptions and comfort, different mathematical models are coupled to building energy and airflow models or specific simulation software [16], [40], [41]. Although such software are often proved to be a good choice between simulation accuracy and simulation time [42], a lack of whole building simulation tools including advanced DSF is highlighted. It is also noted the need of models which are flexible with respect to the development of suitable operation strategies and the implementation of specific mathematical models [43], [44]. Such tools could be adopted by building designers and researchers for detailed and rapid numerical analyses on advanced DSFs, especially during the design phase of NZEBs [1].

In this framework a mathematical model is purposely developed in order to analyze and optimize the design of advanced DSFs integrating photovoltaics and actively controlled shadings (DSF-PV). Such a model is capable to assess the potential that an innovative DSF-PV has on the energy and visual performance of the building. To this aim, the developed flexible, customizable and scalable mathematical model allows one to: i) study novel operation strategies (i.e. natural mechanical and hybrid ventilation, shadings control, heat recovery, etc.) ii) perform suitable parametric analyses for identifying the set of design and operating parameters (including optical thermal and flow properties of the DSF) which optimize the DSF energy, thermal and visual comfort performances.

2 *Modeling*

In this paper an innovative Double Skin Façade integrating Photovoltaic panels (DSF-PV) on the exterior skin of the façade and shading devices within the cavity is modeled. The developed mathematical model, based on a detailed transient finite difference thermal network, is capable to assess the active and passive effects of a DSF-PV on the thermal and visual comfort and energy consumptions of the building in which the system is integrated.

The model also allows the user to perform a parametric analysis, useful for designers to assess the effect of the considered design and operating parameters (design, geometry, optical, thermal and flow properties, etc.) on the performance of the DSF. By means of this procedure, optimal energy efficiency solutions and building design scenarios can be detected. The parameters that can be changed are reported in Table 1.

The developed model gives the opportunity to be used for pre-feasibility studies, in the early stages of the design of a building or of retrofit projects, integrating in this way the PV/T technology in buildings. The integrated with photovoltaics DSF takes full advantage of the cavity and especially of the wind and buoyancy driven air flow inside the cavity, which serves the system in two ways: i) absorbs the heat from the integrated PV in order to decrease their temperature and hence, improves their electrical efficiency; ii) utilizes the preheated air as a source for natural or hybrid ventilation (heating or cooling) for the building. In addition, the air at the top of the cavity can be introduced to the HVAC system as preheated air, in order to reduce the energy consumption, or it can be introduced directly into the building if the comfort levels of the occupants are satisfied, for free heating purposes. The modeled cavity also includes automated roller shades, which help to regulate the heating and cooling space loads and control the daylight levels in the indoor space.

The mathematical numerical model for the assessment of the energy performance of a multi-story DSF-PV has been implemented in MatLab (Mathworks). The whole façade, and, similarly, the wall of a multi-story building are designed as multiple strips made of different materials, e.g. semi-transparent, transparent, and opaque elements. Control volumes are formed between the strips on the exterior skin and those on the interior. The mass entering the control volume is equal to the mass leaving it and in the absence of work and heat transfer, the energy within the control volume remains constant. Automated roller blinds are located in the middle of the cavity and the air can flow on both sides of the shading device placed within the cavity (Figure 1).

2.1 *Positioning of the PV on the Exterior Skin*

The position of the semi-transparent photovoltaics on the DSF-PV is of great importance due to the shading that they provide and the possible blocking of the view. The concept of three section façade [46] is applied for the exterior skin of the developed DSF-PV. The façade in this way is discretized into three different sections starting from the bottom: the spandrel, the viewing section and the daylight section. The opaque photovoltaics (OPV) are integrated on the exterior skin at the spandrel section and the semi-transparent (STPV) at the daylight section. The same height of the spandrel sections is taken into account for the exterior and interior skin facades. In order to take advantage of the shading that the photovoltaics provide to the interior skin and furthermore to the interior zone, the height of the STPV

(HSTPV) is defined by the optimal length of an overhang. The length of an overhang is calculated so that the direct solar radiation is blocked from entering the room on April 15 [47]. Then the part of the overhang that exceeds the length of the cavity is projected on the exterior skin in order to calculate the height of the STPV (HSTPV), having in this way the same effect that an overhang would have (equations 1 and 2) (Figure 2). In addition, because the STPV does allow a part of the solar radiation to be transmitted to the inside, the daylighting levels of the interior space can be improved.

$$L_{ov} = \frac{(H_{wd} + H_{uspd})}{\tan d} \quad (1)$$

$$H_{STPV} = \tan(d) * (L_{ov} - L_{ca}) \quad (2)$$

Where H represents the height of the window and the upper spandrel and L the length of the overhang and the cavity. Starting by the initial design configuration of the exterior skin, it is possible to determine the position of the photovoltaics which optimizes the visual and thermal comfort (providing shading to the adjacent indoor zones), while increasing the electrical efficiency of photovoltaics.

2.2 Transmittance of STPV and Glazing

The calculation of the solar radiation incident on any tilted surface is carried out by taking into account the solar geometry equations [47]. Thus, starting by solar radiation and solar geometry data (e.g. direct normal and diffuse solar radiation, latitude and longitude), imported to the model, the direct and diffuse solar radiation are calculated for the vertical surface of the DSF-PV. The modeling of the transmittance of the semi-transparent photovoltaic and the glazing is determined by their properties. The extinction coefficient and the refractive index are used in order to calculate the angle of refraction and the component reflectivity. These two parameters are used in order to determine the transmittance, reflectance and absorbance of the semi-transparent photovoltaics and the glazing. The semi-transparent photovoltaic is modeled under the assumption that has a uniform transmittance. For this reason, the extinction coefficient (K) times the glazing thickness of the semi-transparent photovoltaic is given by:

$$K_{STPV}L_{STPV} = -\log(\tau_{STPV}) \quad (3)$$

which is a function of the overall normal transmittance of the STPV (τ_{STPV}). The same principals are used in order to model the effective transmittance and absorption of the glazing at the exterior skin and double pane window at the interior skin [48].

2.3 Shadows

The opaque and semi-transparent photovoltaics integrated on the exterior skin, as well as the roller blind that is implemented within the cavity, provide shading to the building and therefore significantly affect the energy balance of the system. The solar radiation is treated by separating the direct and diffuse sources. To address the direct light, the shadow is calculated by the upper and the lower point of the photovoltaic panels or of the roller blind. The vertical distance between the upper or the lower point of the photovoltaic panels and the shade that they provide is given by equation (4) and is a function the cavity width L_{ca} the solar altitude β_s and the surface azimuth a_s :

$$y_{sh} = \frac{L_{ca} \tan \beta_s}{\cos a_s} \quad (4)$$

The area between these points is fully shaded in the case of the opaque photovoltaics and partially shaded in the case of semi-transparent photovoltaics and the roller (Figure 3). If the photovoltaics integrated on the exterior skin shade the roller blind, then the effective transmittance of both of them is calculated for the interior skin. Because the method of control volumes is used for the energy balance and the points where the shadow begins and ends don't always align with the beginning and the end of each control volume, the percentage of the area that is shaded is multiplied with the percentage of the overall transmittance of photovoltaics and roller to give us the total shade at each control volume. As the number of control volumes in which the DSF-PV is subdivided along the vertical direction increases, the upwards or downwards movements of the roller blinds along the cavity can be controlled via smoother movements (i.e. simulating a dimming control). In this model, the height of the blind, and its thermal and optical properties can be either defined by the user or assessed as a function of the energy or comfort criteria. The existence of a roller blind affects the flow of the air inside the cavity, the thermal balance and the shading to the interior skin, as well as the daylight of the indoor zone.

2.4 Thermal Network

The simulation model of the DSF-PV takes into account all of the heat transfer processes, based on a nodal approach. On each node, the heat balance equation is solved and includes heat transfer due to convection, conduction and radiation. Due to the implementation of the roller blind at the middle of the cavity, two sets of explicit finite difference equations are obtained for each node of the adopted thermal network. The first set of equations is used in the case where there is not a roller blind, or the roller blind is folded, taking into account only one airflow inside the cavity (Figure 4), whereas the second set is used when the roller blind splits the cavity into two smaller cavities. This results into two airflows, one in front of the roller blind and one behind it (Figure 5).

The thermal resistance of the roller blind is considered negligible while it is assumed that no air passes through the shade and the air flow at the two sides of the roller blind are assumed to be equal [26].

In order to capture the gradient of the air temperature along the cavity, each element of the multi-story DSF-PV (i.e. the façade, the two air channels, and the wall) is subdivided, along the vertical direction, in n equal control volumes (i.e. n is suitably selected to enhance the accuracy of the simulation results), whose temperatures are calculated through the energy balance method. The multi-story building adjacent to the DSF-PV is also subdivided in z different perimeter thermal zones. Therefore, in each time step t , for each z -th perimeter zone and for each n -th control volume of the façade, the corresponding energy balance equation is calculated as:

$$\sum_{i=n-1}^{n+1} \frac{T_{f,i} - T_{f,n}}{R_{f,i}} + \frac{T_{db} - T_{f,n}}{R_{ext,n}} + \frac{T_{air,n} - T_{f,n}}{R_{ca.ext,n}} + \dot{Q}_{f,n} + \dot{Q}_{rad,n} + \dot{S}_{f,mlt} = 0 \quad (5)$$

Where R_f is the resistance between each node at the exterior layer on the vertical direction, R_{ext} and $R_{ch.ext}$ are the resistances between the façade and the outdoors and between the façade and the air

within the cavity respectively, while \dot{Q} is the thermal load and \dot{S} is the incident solar radiation due to interreflection within the cavity and are explained later in the paper.

The wall separating the cavity from the indoor space is modeled with two nodes: an exterior (facing the cavity) and an interior (facing the indoor space). Thus, n sections (along the vertical direction) for each of these surfaces and n resistive thermal nodes for each story are taken into account. For such nodes, the boundary conditions are the air flowing within the cavity and the indoor air, respectively. Similarly to equation (5), for each perimeter building zone and for each n -th section/node of the exterior and interior wall surfaces, the corresponding energy balance equations are calculated as:

$$\frac{T_{air,n} - T_{wo,n}}{R_{ca,int,n}} + \frac{T_{wi,n} - T_{wo,n}}{R_{wl,n}} + \dot{Q}_{wo,n} + \dot{Q}_{rad,n} + \dot{S}_{w,mlt} = 0 \quad (6)$$

$$\frac{T_{wo,n} - T_{wi,n}}{R_{wl,n}} + \frac{T_{in,k} - T_{wi,n}}{R_{int,n}} + \dot{Q}_{wi,n} = 0 \quad (7)$$

Here, $\dot{Q}_{wo,n}$ and $\dot{Q}_{wi,n}$ represent the effective transmitted solar radiation incident on the exterior and interior surfaces of the wall and R represents the resistance between the layers of the DSF-PV. These include the diffuse solar radiation and the net (transmitted and/or absorbed) beam solar radiation, suitably calculated by taking into account the cast shadows due to the façade surfaces and the roller blinds (section 2.3). The solar beam radiation, \dot{S}_{mlt} , absorbed as diffuse after many reflections by the surfaces facing the cavity (i.e. façade, roller sides, interior skin), is calculated by following the procedure presented in detailed in the next sections [49]. The radiative heat transfer is calculated by taking into account the incident solar radiation and the long wave radiation exchange among the sky vault and the exterior surfaces (equation (8)) and among the interior surfaces comprising the DSF cavity (equation (9)). To this purpose, the view factors and the radiosities of all sections constituting the cavity were properly calculated, as discussed in the next sections. The radiative terms are calculated as:

$$\dot{Q}_{f,n} = [\alpha_{f,n} I_{f,n} + \varepsilon_n \sigma f (T_{sky}^4 - T_{f,n}^4)] A_n \quad (8)$$

$$\dot{Q}_{rad,n} = A_n \sum_{i=1}^N \frac{\varepsilon_i}{1 - \varepsilon_i} (E_n - J_i) \quad (9)$$

Where E is the total emissive power, J is the radiosity and ε is the emissivity of each layer of the DSF-PV.

The wind and buoyancy-driven air flow in the cavity is assumed to be quasi-steady and for each of the n control volumes in which each air cavity is discretized, an energy balance is written. It must be noted that the air temperature of the cavity inside the DSF-PV describes the radiation exchange, convection and mass transfer, including the identification of the heat transfer coefficients.

As reported in previous studies, the temperature profile in a ventilated cavity is exponential [31]. Thus, with the aim to avoid the use of an air temperature profile, the change of energy of each control volume

is assumed equal to the energy transferred to the air by convection. This leads, after solving a first order differential equation of air temperature [31], to the expression:

$$T_{air,n} = \exp\left(-\frac{R_{ca.ext,n}^{-1} + R_{ca.int,n}^{-1}}{\dot{m}c_{p,air}}\right)T_{air,n-1} + \left[1 - \exp\left(-\frac{R_{ca.ext,n}^{-1} + R_{ca.int,n}^{-1}}{\dot{m}c_{p,air}}\right)\right]\left(\frac{R_{ca.ext,n}^{-1}T_{f,n} + R_{ca.int,n}^{-1}T_{wo,n}}{R_{ca.ext,n}^{-1} + R_{ca.int,n}^{-1}}\right) \quad (10)$$

Different boundary conditions are taken into account and no air leakage is assumed in the DSF-PV cavity. It is also assumed that uniform solar radiation is incident on clean exterior surfaces and PV modules are operating at their maximum power point condition.

$$P_{el} = n_{pv}I_f n A_n \quad (11)$$

Where n_{pv} is the PV efficiency, assumed linearly decreasing with the increasing operating temperature [50], taking into consideration the photovoltaic module efficiency at standard test conditions, the photovoltaic module temperature coefficient (β_{PV}) and the cell temperature under standard test conditions (T_{stc}).

$$\eta_{PV} = \eta_{stc}[1 - \beta_{PV}(T_{PV} - T_{stc})] \quad (12)$$

For each z-th indoor space adjacent to the DSF-PV system, its indoor air is assumed as uniform and perfectly mixed. In order to assess the transient effects induced by the thermal mass, a transient lumped parameters heat transfer model is taken into account [51]. Thus, a finite difference thermal network formulation is used to solve equations at each node in which the floor is discretized. Numerical simulations are based on a transient lumped parameters heat transfer model; this type of model enables accurate simulation of transient effects induced by thermal mass. This entails that for each z-th zone, the differential equations describing the energy rate of change of each temperature node of the floor nodes (fl), and of the air node, (in), are solved by explicit finite difference method as follows [1]:

$$T_{fl,z}^t = T_{fl,z}^{t-1} + \frac{\Delta t}{C_{fl,z}} \left(\dot{Q}_{fl,z} + \sum_{k=1}^N \frac{T_{wi,k} - T_{fl,z}^{t-1}}{\bar{R}_{rad,n}} + \frac{T_{in,z} - T_{fl,z}^{t-1}}{\bar{R}_{fl,int}} \right) \quad (13)$$

$$T_{in,z}^t = T_{in,z}^{t-1} + \frac{\Delta t}{C_{in,z}} \left(\dot{Q}_{in,z} + \sum_{k=1}^N \frac{T_{wi,k} - T_{in,z}^{t-1}}{\bar{R}_{rad,n}} + \frac{T_{fl,z} - T_{in,z}^{t-1}}{\bar{R}_{fl,int}} \right) \quad (14)$$

\bar{R}_{rad} and $\bar{R}_{fl,int}$ are the radiative thermal resistances between the internal wall surfaces and the floor and between the internal wall surfaces and the indoor air, respectively. \dot{Q}_{fl} is a heat source at node fl, whereas \dot{Q}_{in} is thermal power to be added to or subtracted from the z-th zone to maintain the indoor air temperature at the desired set-point. In order to determine \dot{Q}_{in} , the indoor air temperatures are firstly calculated in a free-floating regime and then, where heating or cooling is

required, the energy required to maintain the final zone temperature at the set temperature is iteratively assessed.

2.5 Radiosity method

The modeled exterior skin of the DSF-PV consists of three different sections having an opaque, glazing and a semi-transparent photovoltaic (Figure 1). The opaque photovoltaics are expected to perform in higher temperatures than the semi-transparent ones, and both the photovoltaics to have higher temperatures than the glazing. This lack of uniformity on the exterior skin has an effect on the long wave radiation heat exchange and eventually in the solar radiation absorbed within the cavity, which must be accurately taken into account. In addition, in the case where the roller blind is implemented in the middle of the cavity, the radiation exchange between some areas of the exterior and the interior skins are interrupted.

For assessing the radiative heat transfer within the cavity and the solar radiation absorbed by the surfaces of the cavity after multiple reflections, all view factors were properly calculated. The complexity of the radiative model developed for the DSF-PV is mainly because it follows the number of the chosen control volumes which demarcate strips along the width of both skins of the DSF subdividing each surface in N sub-surfaces.

In the implemented model, the double area integration approach is taken into account for the calculation of the fundamental expression for a view factor between isothermal, black-body, diffusely emitting and reflecting surfaces [52]. Each n -th surface is sub-divided into $N_x \times N_y$ rectangular elements (i.e. N_x divisions along the horizontal edge and N_y divisions along the vertical edge) of the same area.

$$F_{i \rightarrow j} = \frac{1}{\pi A_i} \sum_{i=1}^{N_x} \sum_{j=1}^{N_y} \frac{\cos \vartheta_i \cdot \cos \vartheta_j}{r_{ij}^2} \Delta A_i \Delta A_j \quad (15)$$

Where r represents the distance between the two surfaces and the cosines θ_i and θ_j denote the angles between r and the respective normal vectors. The appropriate number of divisions ($N_x \times N_y$) is previously selected such as the difference between the analytical solution of the view factor between the two parallel plates of the DSF [53] and the sum of the n -th view factors calculated by the equation 15 is lower than a specified tolerance.

The view factors between the façade and the reradiating surfaces at the edges of the cavity are calculated according to the geometric correlations for parallel equal rectangular plates and adjacent rectangles [54]. In the cases of the presence of the obstructing roller blind located within the cavity, the view factor between interrupted subsurface are set to be equal to zero. Therefore, in order to determine the view factor between two interrupted cavity sub-surfaces, a suitable algorithm was implemented. Specifically, depending on the roller blind position into the cavity, the two extreme pairs of sub-surfaces of the cavity facades ΔA connected by virtual lines are defined by means of geometric considerations.

The bottom and top of the cavity, as well as the side surfaces, were assumed to be adiabatic and reradiating with a floating temperature distribution. On each sub-surface the radiosity, J_n , is assumed to

be uniform, and the radiative heat flux ($\dot{Q}_{rad,n}$ in equation 9) is related to its temperature (i.e. emissive power, E_n) and to J_n , as it follows:

$$\sigma \cdot T_{f,n}^4 = J_n + \frac{1 - \varepsilon_n}{\varepsilon_n} \cdot \sum_{k=1}^{\bar{N}} F_{n \rightarrow k} \cdot (J_n - J_k) \quad (16)$$

In order to determine the unknown radiosities and temperatures of all the sub-surfaces and surfaces, with $\bar{N} = 2 \cdot N + 4$ of the cavity, a system of \bar{N} linear algebraic equations, in a matrix form, is solved [53].

The solar beam radiation absorbed as diffuse after many reflections by the exterior skin, the interior skin and the roller sides is calculated by following the procedure presented by Athienitis and Stylianou [49]. The total beam radiation absorbed after many reflections by a n -th surface is given by:

$$S_{mlt} = A_n \sum_{k=1}^{\bar{N}} F_{nk}^d \cdot Q_k \cdot I_{dir} \cdot f_{w,k} \quad (17)$$

Where the portion of the glazing surfaces directly illuminating the k surface, $f_{w,k}$, is defined starting by the knowledge of the cast shadows (as reported in Section 2.3). The transfer factor, F_{nk}^d , is calculated as the fraction of diffuse solar radiation emitted by surface k which is absorbed by surface n and is calculated as:

$$F_{nk}^d = A_{abs} \cdot F_{nj} \cdot (I_{jn} - \rho_j \cdot F_{jk}) \quad (18)$$

where A_{abs} is a diagonal matrix with the surfaces absorptance equal to its diagonal, F_{nj} is the view factor, I_{jn} is the identity matrix.

2.6 Heat transfer coefficients

The local Nusselt numbers (Nu) are used in order to represent the convective heat transfer coefficients along the cavity height. Nusselt number correlations developed by Liao et al. [30] for the façade and internal side are used:

$$Nu_{ca,ext} = (0.011Re + 62.856)e^{-0.475 \frac{H}{L_{ca}}} + (2.766 \times 10^{-3})Re + 5.58 \quad (19)$$

$$Nu_{ca,int} = (0.109Re - 124.34)e^{(-1.635 \times 10^{-5} Re - 0.593) \frac{H}{L_{ca}}} + (4.098 \times 10^{-3})Re + 3.896 \quad (20)$$

By using the definitions of Nusselt and Reynolds number, the local convective heat transfer coefficients were calculated.

$$Nu = \frac{h_{ca} D_{ca}}{K_{air}} \quad (21)$$

$$Re = \frac{\rho_{air} V_{air} D_{ca}}{\mu} \quad (22)$$

The exterior convective heat transfer coefficients caused by the wind are calculated based on the equation developed by Emmel (2007).

$$\begin{aligned} h_{out} &= 5.15 V_w^{0.81} & \theta &\leq 22.5^\circ \\ h_{out} &= 3.34 V_w^{0.84} & 22.5^\circ &< \theta \leq 67.5^\circ \end{aligned} \quad (23)$$

$$\begin{aligned}
h_{out} &= 4.78V_w^{0.71} & 67.5^\circ < \theta \leq 122.5^\circ \\
h_{out} &= 4.05V_w^{0.77} & 122.5^\circ < \theta \leq 157.5^\circ \\
h_{out} &= 3.54V_w^{0.76} & \theta > 157.5^\circ
\end{aligned}$$

Where V_w is the wind velocity that has been adjusted for height above ground. This general equation is not taking into account the surface roughness.

2.7 Flow network

Taking into consideration the temperature distribution of the air inside the cavity, as well as the wind velocities and directions, the airflow inside the cavity can be easily determined by means of the simulation model. Moreover, it is also possible to manually set a desired airflow rate inside the cavity, enabling in this way the mechanical ventilation which assists the stack and wind effects. In fact, the flow of the air inside the cavity can be naturally and mechanically driven. The airflow inside the cavity caused by natural effects such as stack and wind effects:

$$\Delta P_{nat} = \Delta P_{th} + \Delta P_w \quad (24)$$

Pressure difference due to stack effect related to the temperature difference between the ambient temperature and the temperature of the air within the cavity is given by:

$$\Delta P_{th} = 0.5\rho_{air}gH_{ca} \left[\frac{T_{m_{ca}} - T_{out}}{T_{ca}} \right] \quad T_{m_{ca}} - T_{out} \geq 0 \quad (25)$$

$$\Delta P_{th} = 0.5\rho_{air}gH_{ca} \left[\frac{T_{m_{ca}} - T_{out}}{T_{out}} \right] \quad T_{m_{ca}} - T_{out} < 0 \quad (26)$$

Where $T_{m_{ca}}$ is the average temperature of the air inside the cavity. The pressure drop due to wind effect is given by the equation:

$$\Delta P_w = \Delta C_p 0.5\rho_{air}V_w^2 \quad (27)$$

For this equation, the velocity of the air measured at a height of 10m above ground is used. The pressure coefficients, determined experimentally by Lou et al. [56] for twelve wind angles over 360°, are used in order to calculate, via interpolation, the difference between the pressure coefficients at the exterior and the interior skin of the DSF-PV (ΔC_p).

$$V_{ca,th} = \frac{C_d}{A_{ca}} \sqrt{\Delta P_{nat}} \quad \Delta P_{nat} \geq 0 \quad (28)$$

$$V_{ca,th} = -\frac{C_d}{A_{ca}} \sqrt{|\Delta P_{nat}|} \quad \Delta P_{nat} < 0 \quad (29)$$

The used orifice equation employs a discharge coefficient of $C_d = 0.62$ for a flow through sharp edged rectangular objects.

The total pressure drop caused by thermal, wind and mechanical systems is described by:

$$\Delta P_{tot} = \Delta P_{nat} + \Delta P_{mech} \quad (30)$$

If natural airflow inside the cavity does not reach the desired airflow rate, then the fans at the top of the DSF-PV start to operate.

The pressure drop due to the mechanical system is calculated by the equation:

$$\Delta P_{mech} = \left(\frac{V_{ca} A_{ca}}{C_f} \right)^2 - \Delta P_{nat} \quad (31)$$

2.8 Energy Calculation

The electricity consumption for heating and cooling purposes is calculated by taking into account the electricity consumption of air-to-water heat pumps/chillers that either supply or remove heat from the perimeter zones. In the simulation model, the Coefficient Of Performance (COP) and the Energy Efficiency Ratio (EER) of the selected heat pump/chiller devices vary as a function of the occurring operating conditions as defined by the manufacturers. Specifically, COP and EER are calculated as a function of the part load ratio, the ambient temperature and the temperature of the condenser or the evaporator, by following a lookup data approach [57]. The amount of electricity needed for the operation of the heat pump, $P_{HP/CH}$, is calculated by the heating or cooling demand, \dot{Q}_{in} , as:

$$P_{HP/CH} = \frac{\dot{Q}_{in}}{COP/EER} \quad (32)$$

A simple radiosity daylight model [58] is used to assess the illuminance levels on the work-plane and the energy consumed in order to artificially light this area with lamps. When daylight is not enough to meet the set-point selected (300 lx), dimmable LED lighting that provides additional light to reach the required illuminance on the work-plane is assumed. The equation (33) is used to calculate the electricity consumed for the artificial lighting of the work-plane by using the average illuminance on the work-plane.

$$P_{lamps} = \frac{(E_{setpoint} - E_{average}) A_{workplane}}{n_{lamps}} \quad (33)$$

The difference between the desired illuminance set-point and the average illuminance on the work plane are calculated for each time step and for the cases where the daylight is not adequate to light the room during the working hours, the lamps are assumed to be operating. The electricity consumption due to the lighting system is calculated by taking into account dimmable LED lightning lamps with a luminous efficacy of 100lm/W.

An important fraction of the electricity consumption comes from the operation of the fans that assist the flow inside the cavity. The amount of the electrical power due to fans operation is calculated starting by the assessment of the pressure drop due to the mechanical system, ΔP_{mech} , the air flow rate (\dot{m}_{ca}), and the fan efficiency (n_{fan}), as:

$$P_{fan} = \frac{\dot{m}_{ca} \Delta P_{mech}}{n_{fan}} \quad (34)$$

3 Validation procedure

Experimental values from previous studies are used for the verification of the simulation model [59]. For this comparison the experiments held on a test-hut built up in Concordia University (Montreal, Canada)

and collected in March 2004 are used. Simulations were carried out by taking into account the same boundary conditions considered by Liao et al. [59]. The physical features of the considered opaque PV modules are reported in Table 2. The opaque PV panels that are integrated on the exterior skin are located at a distance of 0.1 m from the insulated interior wall (both of them have a height of 1 m).

For validation purposes a comparison is carried out between the experimental and the simulated results related to the temperature of the opaque PV panel (T_{pv}) and the interior wall (T_{ins}). The results of this analysis are presented in Table 3. A good agreement between predicted and experimental results is obtained (the detected error is within a range of 1.5°C). The only exception is observed when the incident solar radiation is significantly high. In this case the temperature difference between predicted and measured results is lower than 4°C. Note that such differences do not drastically affect the calculated efficiency of the PV panels. In particular, being the simulated temperatures higher than the measured ones, a conservative underestimation of the calculated PV electricity production is obtained by equations (11) and (12).

This difference could be credited to the accuracy and precision of the measuring instruments, the unknown insulating value of the experimental set-up and also to the unknown wind velocity occurring during the experimental procedure.

4 Case study

A set of simulations is suitably carried out, in order to show the capabilities of the simulation model to assess the energy performance, to found out advantages and drawbacks of the modelled innovative DSF-PV. The simulation were performed over a time horizon of one year for the heating dominated climate of Montreal (Canada). A one-hour time step was selected, compatible with the Typical Meteorological Year data files (TMY) used as a source for the weather input data. The simulated DSF-PV operates for a perimeter office building, where the indoor conditions follow a normal weekday schedule from 08:00 to 18:00 and the temperature is free to fluctuate between 21 and 24°C. The operation of a HVAC system is required in order to maintain the indoor air temperature within such range. The simulations are carried out by assuming two-pipe fan-coils to be the building terminal units, with supply temperatures of 45 °C for the heating mode and 7 °C for the cooling mode.

A Double Skin Façade integrating Photovoltaic panels (DSF-PV) is implemented on the South façade of a reference building. The area covered by the opaque PV panels (OPV) is about 55% of the total south-facing surface, with a nominal OPV efficiency of 20%. The reference office building described by Reinhart et al. [60] was used for the design of the interior zone. In each indoor space it is assumed that the plug load factor is 3.55 W/m². Each workstation is 12.5 m², all the occupants use notebooks and one printer is assigned for every ten occupants [61]. A three floor office building with a rectangular East-West oriented shaped plant (3.6 × 8.2 m) is taken into account for the simulations. The height of each intermediate floor of the building is 2.8 m. The bottom spandrel is 1.0 m high, the window is 1.5 m high, and the upper spandrel is 0.3 m high, for a window-to-wall ratio of 55%. The investigated range of the air cavity thickness of the integrated DSF-PV is between 0.1 and 0.6 m. The roller blind is placed in the middle of the DSF-PV air cavity. The solar transmittance of the roller is set to 10% and the related reflectance is 50%. The investigated solar transmittances of the semi-transparent PV panels (STPV) are 30%, 50% and

70%. In this analysis, the roller blind is implemented at the viewing section, i.e. it starts directly underneath the STPV panels integrated at the exterior skin and can expand downward till the spandrel section, as shown in Figure 6.

In this study, a multi-story DSF-PV model was simulated by taking into account different roller set-ups, aiming at analyzing the effect of the adoption of the motorized blinds on the energy performance of the DSF-PV. The shading effects of the roller can be simulated for different positions along the cavity. Here, five different shading positions (R_s) are modelled. One set-up refers to the roller blind completely shading the viewing section ($R_s = 100\%$ shading), another one refers to a rolled-up roller blind ($R_s = 0\%$ shading), as shown in Figure 6. In addition, three modulated positions ($R_s = 25\%$, 50% and 75%) are also considered. Here, it is possible to observe that the downward movement of the roller blind is allowed along the window viewing section only, without directly shading the daylight one.

To assess the impact of the velocity of the air flowing inside the DSF-PV cavity (V) on the system performance, different set-points (i.e. V_{sp} between 0.3 and 1 m/s) were taken into account. Different ventilation modes of the air flowing inside the cavity such as natural, mechanical and hybrid regimes can be simulated. If the natural ventilation is not capable to meet the required velocity, the stack and wind effects are boosted through the mechanical ventilation system. For the simulated fan driven ventilation system, an average electrical efficiency of the fan n_{fan} , equal to 70% is assumed.

Different operating strategies are taken into account in the developed case study according to the fan operation and roller blinds layouts. Specifically, three air flow modes can be alternatively simulated and applied in different scenarios: i) air flow assisted by fans (MVent); ii) natural convection flow (NVent); iii) no flow (Closed). According to such occurrences ten different operating strategies for the DSF-PV are implemented in the code (Table 4). In addition, five different strategies have been developed for the use of the roller blinds, based only on the heating and cooling needs of the adjacent to the DSF-PV zone (Table 5). Additional strategies will be developed by taking into consideration the illuminance levels on the work-plane, as a result of the shading provided by the roller blind.

The heat recovered by the DSF-PV air cavity is exploited to enhance the COP of the heat pump (HP), with the aim to minimize its seasonal variation. During winter the DSF-PV is coupled with the evaporator side of the air-to-water HP to reduce space heating demand. DSF preheated air is mixed with outdoor air, prior to entering the heat pump, to ensure adequate airflow to the evaporator. For the selectable heat pump / chiller, heating and cooling capacity and performance data are assessed as a function of the water and air inlet temperatures. Simulations are carried out by taking into account an inverter driven reversible heat pump with a COP ranging between 1.35 and 5.20, and an EER ranging between 2.74 and 9.74. These data are estimated based on manufacturers and, for the carried out analysis, are provided for the CLIVET WSAN-XIN 101 (Excellence series) HP, which can operate under part load conditions. The equipment's water flow rate are set at constant value, whereas air flow rates can be also varied as a function of the part load conditions. Nevertheless, the selected heat pump /chiller is not allowed to operate at less than 40% of its maximum capacity. Outside the operation limit conditions (PRL, temperatures, etc.), HP performance are not affected by the compressor inverter frequency and the air flowrate remains unchanged. Finally, during the heating mode, if the HP air inlet temperature is lower than minimum allowed temperature, or the HP capacity is not sufficient to supply the space heating requirements, an electrical back-up is turned on. The heat pump performances provided by manufactures' are in accordance with the standard EN14511 (2013, Air conditioners, liquid chilling

packages and heat pumps with electrically driven compressors for space heating and cooling), including defrost cycles losses.

5 Results and discussion

The results obtained through the simulation of the developed mathematical model are analyzed and the influence of the main design and operating parameters on the system energy performance is discussed.

5.1 Thermal analysis: general considerations and roller blind effects

In Figure 7 the temperatures of the air cavity as a function of time and cavity length (for a three floor building façade) is shown for a sample summer day (July 7th). Simulations are carried out for $V_{sp} = 0.5$ m/s and $R_s = 0\%$ (i.e. rolled up blinds).

An air cavity temperature growth is obtained by increasing the height of the building façade. Higher temperature increments (steeper temperature gradients) are observed in correspondence of the opaque photovoltaic (OPV) panels within the façade. This result is due to the higher temperatures of the OPV panels versus the rest of the exterior skin.

The effects of roller blinds on the air cavity temperatures are shown in Figure 8, where the case fully rolled down blinds ($R_s = 100\%$) is presented. By comparing Figure 7 and Figure 8 it is possible to observe that the roller blinds contribute to a certain increase of the air cavity temperature, especially in correspondence of the OPV panels where remarkable air temperature growths are detected. As expected, simulation results also show that for a given incident solar radiation, the lower the inlet air temperature, the higher the temperature difference between the air at the bottom inlet and the upper outlet louvers. It should be noted that the outlet louvers are not shown in the figures for sake of brevity.

In Figure 9, the time histories of the average temperatures of the opaque (T_{opv}) and semi-transparent PV (T_{stp}) panels, as well as the average temperatures of the ambient air (T_{out}) and cavity (T_{air}) are reported together with the façade incident solar radiation (I_{tot}) for four typical summer days (June 29th - July 2nd). The obtained results are referred to a minimum velocity set-point of the air flowing within the cavity (V_{sp}) set to 0.5 m/s during daytime (from 8:00 to 18:00, beyond such time interval the cavity is considered to be naturally ventilated only). In Figure 9 it is possible to observe that in the building perimeter zone the indoor air temperature is maintained to the cooling set-point (24°C) between 8:00 to 18:00 whilst is in free floating during the rest of the time. The maximum incident solar radiation on the building façade (I_{tot}) ranges between 200 and 450 W/m², whereas the ambient temperature fluctuates between 11 and 33°C. As expected, the temperatures of the PV panels and air cavity are strongly affected by these parameters. The temperature peaks of both the PV panels (i.e. opaque OPV and semi-transparent STPV) almost correspond to the peaks of the façade incident solar radiation. In summer, T_{opv} approaches 40°C, being averagely 15°C higher than the ambient air temperature. Conversely, T_{stp} is remarkably lower than T_{opv} because of the lower STPV panels' absorptance with respect to the one of the OPV panels (the reported results are referred to a transmittance of STPV panels equal to 30%).

The obtained air cavity temperature (T_{air}) increment is low and almost follows the fluctuation of the ambient temperature (T_{out}) being only weakly influenced by the incident solar radiation (I_{tot}). This result is due to the minimum velocity set-point for the air flowing within the cavity ($V_{sp} = 0.5$ m/s). During the night, the temperature of the PV panels is slightly lower than the temperature of the ambient/cavity air. This result is due to the infrared radiation exchanges between such high emissivity surfaces and the sky vault.

5.2 Parametric analysis

The results of a suitable parametric analysis carried out are reported in this section. The analysis aims to identify the parameters that minimize the heating or cooling energy peaks and demands, while maximize the electricity production of the building integrated PV panels (BIPV).

5.2.1 Air flow control effect

The above described strategies that combine natural, mechanical and hybrid ventilation modes in the air cavity of the double skin façade were simulated for a cavity thickness (L_{ca}) equal to 0.5 m without using roller blinds ($R_s = 0\%$). Figure 10 reports the average yearly electricity consumption per floor necessary for heating and cooling, calculated for all the above mentioned airflow and fan operation strategies (presented in Table 4).

For the heating dominated climate zone of Montreal (Canada), and from the energy efficiency point of view, Strategy 10 (Table 4) is shown to be the optimal. In fact, when the indoor zone requires to be heated, the air cavity closes and, the double skin façade acts as a buffer thermal insulating zone. Conversely, when cooling is needed, the cavity is ventilated through fans in order to reach the velocity set-point (V_{sp}) of 0.5 m/s. For the considered climatic conditions, the selected minimum air cavity velocity set-point cannot be reached only by the pressure difference due to thermal buoyancy and wind. The additional pressure difference has to be provided by fans, which assists the stack and wind effects. Finally, in the mid-season, when the room indoor air temperature is between the heating and cooling set-points (21 and 24°C respectively), the cavity is naturally ventilated. The second preferred strategy, according to the energy performance, is Strategy 7 (Table 4). Here, the difference between the average temperature of the air within the cavity (T_{ca}) and the temperature of the air within the room is used to determine when the cavity will be mechanically assisted and when it will be closed. Almost similar energy performances are presented by strategies 3, 8 and 9 where a yearly electricity demand always lower than 611 kWh/m² is achieved.

During the heating season, the waste heat from the double skin façade can be recovered and supply the evaporator of the considered heat pump with the outlet air from the DSF-PV, enhancing in this way its COP. As a function of the selected fan operation strategy, different HP performances can be achieved. In Figure 11, three sample days (January 19th – 21st) are presented, showing the differences of an hourly COP for the cases of i) heat recovery mode ii) reference mode. In the heat recovery mode, air from the DSF-PV is delivered to the HP evaporator by taking into account the fan Strategy 5 (table 4) and in the reference mode, the evaporator is supplied by outdoor air only. At the upper side of Figure 11, the yearly variations of the COP for such operation modes are also displayed. Results are obtained by taking into account velocity set-point (V_{sp}) and cavity thickness (L_{ca}) equal to 0.5 m/s and 0.5 m, respectively.

The COPs calculated for Strategy 5 are significantly higher than those achieved without heat recovery and the maximum increment of COP ranges from 0.25 to 0.5.

The obtained COP versus the outdoor air temperature (T_{out}), calculated for the Strategy 5 fan operation, compared to the reference case, is shown in Figure 12. The spread of the COP is due to the different part load ratios and supplying air temperatures (in case of DSF heat recovery) which can occur at the same T_{out} . From Figure 12, it is possible to notice an overall increase of the COP calculated in case of Strategy 5 with respect to the reference case.

The percentage difference of the COP increases up to a maximum value of 50% and is achieved at very low temperatures (lower than -15°C). It ranges from 20 to 35% for ambient temperatures from -10 to 8°C and it becomes negligible for T_{out} higher than 12°C . The COP trend obtained with Strategy 5 is similar to those achieved for Strategy 1 and 4, under the same simulation assumptions. The air flow leaving the DSF is supplied to the HP evaporator only if it has temperatures higher than T_{out} that occur mainly during daily hours. On the contrary, there is no significant increase for the COP for Strategy 7, as shown in Figure 12. In fact, the COP trend achieved through Strategy 7 is similar to that of the reference case (with the exception of few points around $T_{out} 10^{\circ}\text{C}$). This is due to the weather conditions which rarely allow the cavity outlet air temperature (T_{ca}) to surpass the indoor air temperature (T_{room}). Note that for Strategy 7 the DSF cavity is always closed for $T_{ca} \leq T_{room}$ (Table 4). This can be also observed by analyzing the percentage distributions of occurrences of the COP, calculated for all the investigated fan operation strategies, reported in Table 6. The percentage frequency of the COP falling within the interval 3.5 – 4.5 increases from 3.4% for the reference case to 12.7% for Strategy 1, 4 and 5. For this interval, the maximum is detected for Strategy 2 (13.5%), due to the higher temperatures of air flowing through the naturally ventilated cavity. On the other hand, Strategy 2 requires the use of the auxiliary heater (AH) for about 0.6% of the heating time, while Strategy 7 and 8 show the highest percentage frequency distribution related to the AH (about 3.7%). This is due to the lower airflow ventilation rates obtained by the naturally ventilation mode vs. the mechanical /hybrid ones.

For all the above described simulation results, the heat pump was suitably sized by taking into account the thermal load of the simulated three-floor building. The selected HP is capable to operate at severe outdoor winter conditions, providing remarkable heating capacity at low evaporating temperatures (i.e. varying from -20 to 18°C). As the selected heat pump is not allowed to operate at less than 40% of its maximum capacity, it could be interesting to analyze the system performance when multiple running heat pumps are considered, with the aim to exploit the heat recovery by taking advantage of part load operation (PLR).

5.2.2 Roller blind control effect

According to the roller blind shading strategies presented in Table 5 the calculated average yearly electricity consumption per floor necessary for heating and cooling is reported in Figure 13. The results of the carried out case-investigation refer to an air cavity thickness (L_{ca}) equal to 0.5 m and to a three-floor DSF-PV building.

The most convenient roller blind strategy to minimize the electricity used for heating and cooling demands is Strategy 5 (Table 5). By such roller blind operation strategy, the roller blinds are open during the daytime of the heating season ($R_s = 0\%$) and closed during the daytime of the cooling one ($R_s =$

100%) and always closed during the night ($R_s = 100\%$). In this case, the calculated electricity consumption is about 603 kWh/y. With the exception of Strategy 4, the remaining ones require electricity consumptions higher than 606 kWh/y.

In addition, the incident solar radiation reaching the window area of the interior surface of the DSF was investigated for five different roller blind layouts. The window shaded viewing portion was varied by taking into account an R_s equal to 25%, 50%, 75% and 100% and the case where no roller blind was considered within the cavity of the DSF-PV ($R_s = 0\%$). The results of this analysis are shown in Figure 14. The effect that the opaque and semi-transparent PV panels as well as the roller blinds have on the incident solar radiation on the interior skin of the DSF can be observed in terms of percentage incident solar radiation.

Such incident solar radiation is almost blocked during the summer months, avoiding the overheating effects. For example in June, by modulating the roller blind from $RS = 0\%$ to $RS = 100\%$, the transmitted solar radiation ranges from 14% to 8%. Conversely, during winter, solar heat gains can enter the room. For example in January, by modulating roller blinds from $RS = 0\%$ to $RS = 100\%$, the transmitted solar radiation ranges from 68% to 29%. Although the roller blinds shade the window viewing section, there is sufficient incident solar radiation at the top daylight section of the interior skin. In this way, glare effects can be avoided whereas occupants' visual comfort and room daylight autonomy are increased.

5.2.3 *Air cavity thickness effect*

In the developed simulation model the top floor of the DSF-PV is simulated in a different way versus the two bottom floors. For the top floor, the shading from the top of the DSF-PV is also taken into account.

Regarding the electricity consumption for lighting, the related difference detected between top and intermediate floor is reported in Figure 16 as a function of the air cavity thickness (L_{ca}). The results are referred to a three-storey building DSF-PV with a 30% visible transmittance semi-transparent PV panels without a shading device implemented within the cavity ($RS = 0\%$). In addition, an air cavity velocity set-point of 0.5 m/s, Strategy 10 for the fan operation and Strategy 5 for roller blind control are simulated. In this figure, it can be observed that for a small cavity thickness ($L_{ca} = 0.1$ m) the electricity consumption for artificial lights is almost the same for all the simulated building floors. In this case the transmitted solar radiation is practically equivalent for all the building floors. By increasing the cavity thickness, lower solar radiation is obtained for the top floor and, thus, a growth of the electricity demand for lighting is observed. At the maximum air cavity thickness simulated ($L_{ca} = 0.6$ m) the calculated difference between the electricity consumption for the top and intermediate floors reaches about 12.5%, as shown in Figure 15, which also shows the electricity consumption due to artificial lights at the top and intermediate story as a function of the cavity thickness.

In Figure 16 the calculated average yearly electricity consumption per floor required for heating, cooling, artificial lights and air cavity fans are reported as a function of the cavity thickness. In the same figure, the overall electricity demand is also depicted. In Figure 17 it can be observed that the increase of the air cavity thickness implies a growth of the related air flow rate. For this reason, higher building envelope thermal losses are obtained (decreasing buffer zone effect of the air cavity), with a consequent increase of the heating demand and a slight decrease of the cooling demand. The increase of the air flow rate requires higher electricity consumption of the air cavity fans and the overall yearly electricity

presents a weak growth as the cavity width increases. In addition, the highest electricity consumption is detected for the building heating, because of the considered heating dominated climate of Montreal (Canada),

5.2.4 Electricity balance for different perimeter zone floor areas

In Figure 17 the electricity balance between the building consumption and the PV panels production is reported as a function of the semi-transparent PV panel transmittances (0.3, 0.5 and 0.7) and the floor area of the building perimeter zone. In this analysis, the area of the PV panels area is constant, since the width of the façade does not change, whilst the indoor space depth varies. By increasing this parameter, a growth of the electricity consumption due to space heating, cooling, daylighting and appliances is obtained. In Figure 17, it can be observed that a building exportation of electricity can be always reached for building perimeter zone areas lower than 27 m². Such threshold (corresponds to a PV panel transmittance of 70%) can be increased for lower PV panel transmittances. Since the obtained electricity production of the PV panels is about 26.3 kWh/m²year, the overall energy balance throughout the year is always positive.

The yearly electricity consumptions due to heating, cooling, lighting, fans and plug loads are reported in Table 7 and in Figure 18. Also in this case, such results are referred to unshaded windows, V_{sp} equal to 0.5 m/s, Strategy 10 for fan operation, and Strategy 5 for roller blind control.

Of the total electricity consumption, 42% is due to heating, 37% is for plug loads while about 10% is for cooling and lighting. It is noteworthy to observe that the electricity consumption due to the air cavity fans is less than 1%. In addition to the low fan speed ($V_{sp} = 0.5$ m/s), such result is due to the closed DSF-PV cavity during the heating period (fan operation Strategy 10).

6 Conclusion

In this paper a numerical model of a Double Skin Façade integrating opaque and semi-transparent PV panels (DSF-PV) is presented. The paper also includes a detailed description of the mathematical equations and of the procedure followed in order to simulate the thermal and energy performance of the multi-story DSF-PV system. With the aim to show the capability of the numerical model, a set of simulations was carried out for a winter week and a whole year by taking into account different DSF cavity fan operation strategies and roller blind set-ups. A particular attention was paid to the assessment of the influence of the roller blind operation on the thermal and energy performances of the double skin façade.

Simulations were carried out for a high-rise office building equipped with this innovative DSF-PV system for the weather climate of Montreal (Canada). The obtained simulation results show that:

- the solar radiation is almost blocked during the summer months by the opaque photovoltaics integrated at the exterior skin, preventing overheating effects;

- the integrated photovoltaic panels can provide significant amount of energy to heat or cool the interior adjacent zones, by supplying approximately 26.3 kWh/m²/year of solar electricity;
- by suitably reducing the PV panel transparencies, the amount of electricity production can be sufficient to balance the energy consumptions throughout the year due to space heating, cooling, daylighting and appliances. For the investigated building perimeter zone, the use of semi-transparent PV (transmittance 70%), allows reaching the nearly zero energy goal for an indoor space area up to 27 m².

Finally, the developed simulation model allows assessing the performance of a double skin façade integrated with photovoltaics, in order to aid the design of net-zero energy buildings. The simulation model also allows performing parametric and sensitivity analyses and it can be used for pre-feasibility studies at the design phase of new buildings or for retrofit projects.

Acknowledgments

The authors acknowledge the support of the Natural Sciences and Engineering Research Council of Canada (NSERC) through a NSERC/Hydro Quebec Industrial Chair. They also wish to acknowledge the scientific support of the Action TU1205 (Building Integration of Solar Thermal Systems, BISTS) of the European COST (Cooperation in Science and Technology), Transport and Urban Development (TUD).

References

- [1] A. Athienitis and W. O'Brien, *Modeling, Design, and Optimization of Net-Zero Energy Buildings*. 2015.
- [2] X. Cao, X. Dai, and J. Liu, "Building energy-consumption status worldwide and the state-of-the-art technologies for zero-energy buildings during the past decade," *Energy Build.*, vol. 128, pp. 198–213, 2016.
- [3] A. Buonomano, G. De Luca, U. Montanaro, and A. Palombo, "Innovative technologies for NZEBs : An energy and economic analysis tool and a case study of a non-residential building for the Mediterranean climate," *Energy Build.*, vol. 121, pp. 318–343, 2016.
- [4] S. Monteiro, R. Mateus, L. Marques, and M. Ramos, "Solar Energy Materials & Solar Cells Contribution of the solar systems to the nZEB and ZEB design concept in Portugal – Energy , economics and environmental life cycle analysis," *Sol. Energy Mater. Sol. Cells*, vol. 156, pp. 59–74, 2016.
- [5] I. E. A. IEA, "Expert Guide Part 2 Responsive Building Elements," 2009.
- [6] I. Sartori, A. Napolitano, and K. Voss, "Net zero energy buildings: A consistent definition framework," *Energy Build.*, vol. 48, pp. 220–232, 2012.
- [7] R. A. Agathokleous and S. A. Kalogirou, "Double skin facades (DSF) and building integrated photovoltaics (BIPV): A review of configurations and heat transfer characteristics," *Renew. Energy*, vol. 89, pp. 743–756, 2016.
- [8] D. Saelens, J. Carmeliet, and H. Hens, "Energy Performance Assessment of Multiple-Skin Facades," *HVAC&R*

- Res.*, vol. 9, no. 2, pp. 167–185, 2003.
- [9] E. Gratia and A. De Herde, “Are energy consumptions decreased with the addition of a double-skin?,” *Energy Build.*, vol. 39, pp. 605–619, 2007.
- [10] M. a. Shameri, M. a. Alghoul, K. Sopian, M. F. M. Zain, and O. Elayeb, “Perspectives of double skin façade systems in buildings and energy saving,” *Renew. Sustain. Energy Rev.*, vol. 15, no. 3, pp. 1468–1475, 2011.
- [11] G. Quesada, D. Rousse, Y. Dutil, M. Badache, and S. Hallé, “A comprehensive review of solar facades. Transparent and translucent solar facades,” *Renew. Sustain. Energy Rev.*, vol. 16, no. 5, pp. 2643–2651, 2012.
- [12] S. Kala, T. Stathopoulos, and K. Suresh Kumar, “Wind loads on rainscreen walls: Boundary-layer wind tunnel experiments,” *J. Wind Eng. Ind. Aerodyn.*, vol. 96, no. 6–7, pp. 1058–1073, 2008.
- [13] F. Favoino, F. Goia, M. Perino, and V. Serra, “Experimental analysis of the energy performance of an ACTIVE, REsponsive and Solar (ACTRESS) facade module,” *Sol. Energy*, vol. 133, pp. 226–248, 2016.
- [14] S. Barbosa and K. Ip, “Perspectives of double skin façades for naturally ventilated buildings: A review,” *Renew. Sustain. Energy Rev.*, vol. 40, pp. 1019–1029, 2014.
- [15] E. Gratia and A. De Herde, “Is day natural ventilation still possible in office buildings with a double-skin façade?,” *Build. Environ.*, vol. 39, pp. 399–409, 2004.
- [16] E. Gratia and A. De Herde, “Natural ventilation in a double-skin facade,” *Energy Build.*, vol. 36, no. 2, pp. 137–146, 2004.
- [17] E. Gratia and A. De Herde, “Natural cooling strategies efficiency in an office building with a double-skin façade,” *Energy Build.*, vol. 36, no. 11, pp. 1139–1152, 2004.
- [18] A. de Gracia, L. Navarro, A. Castell, and L. F. Cabeza, “Energy performance of a ventilated double skin facade with PCM under different climates,” *Energy Build.*, vol. 91, pp. 37–42, 2015.
- [19] A. Fallahi, F. Haghghat, and H. Elsadi, “Energy performance assessment of double-skin facade with thermal mass,” *Energy Build.*, vol. 42, no. 9, pp. 1499–1509, 2010.
- [20] E. Gratia and A. De Herde, “The most efficient position of shading devices in a double-skin facade,” *Energy Build.*, vol. 39, pp. 364–373, 2007.
- [21] H. Manz, “Total solar energy transmittance of glass double facades with free convection,” *Energy Build.*, vol. 36, no. 2, pp. 127–136, 2004.
- [22] D. Saelens, S. Roels, and H. Hens, “Strategies to improve the energy performance of multiple-skin facades,” *Build. Environ.*, vol. 43, pp. 638–650, 2008.
- [23] V. Gavan, M. Woloszyn, F. Kuznik, and J. J. Roux, “Experimental study of a mechanically ventilated double-skin facade with venetian sun-shading device: A full-scale investigation in controlled environment,” *Sol. Energy*, vol. 84, no. 2, pp. 183–195, 2010.
- [24] W. Pasut and M. De Carli, “Evaluation of various CFD modelling strategies in predicting airflow and temperature in a naturally ventilated double skin faade,” *Appl. Therm. Eng.*, vol. 37, pp. 267–274, 2012.
- [25] M. Coussirat, A. Guardo, E. Jou, E. Egusquiza, E. Cuerva, and P. Alavedra, “Performance and influence of numerical sub-models on the CFD simulation of free and forced convection in double-glazed ventilated facades,” *Energy Build.*, vol. 40, no. 10, pp. 1781–1789, 2008.

- [26] N. Safer, M. Woloszyn, and J. J. Roux, "Three-dimensional simulation with a CFD tool of the airflow phenomena in single floor double-skin facade equipped with a venetian blind," *Sol. Energy*, vol. 79, pp. 193–203, 2005.
- [27] Y. Ji, M. J. Cook, V. I. Hanby, D. G. Infield, D. L. Loveday, L. Mei, Q. Building, T. Gateway, and L. L. E. Uk, "CFD MODELLING OF DOUBLE-SKIN FAÇADES WITH VENETIAN BLINDS Institute of Energy and Sustainable Development , De Montfort University , Centre for Renewable Energy Systems Technology , Department of Electronic and Electrical Department of Civil and Building ," pp. 1491–1498, 2007.
- [28] X. L. Xu and Z. Yang, "Natural ventilation in the double skin facade with venetian blind," *Energy Build.*, vol. 40, pp. 1498–1504, 2008.
- [29] Z. Zeng, X. Li, C. Li, and Y. Zhu, "Modeling ventilation in naturally ventilated double-skin facade with a venetian blind," *Build. Environ.*, vol. 57, pp. 1–6, 2012.
- [30] L. Liao, a. K. Athienitis, L. Candanedo, K.-W. Park, Y. Poissant, and M. Collins, "Numerical and Experimental Study of Heat Transfer in a BIPV-Thermal System," *J. Sol. Energy Eng.*, vol. 129, no. 4, p. 423, 2007.
- [31] R. Charron and A. K. Athienitis, "Optimization of the performance of double-façades with integrated photovoltaic panels and motorized blinds," *Sol. Energy*, vol. 80, pp. 482–491, 2006.
- [32] J. H. Yoon, J. Song, and S. J. Lee, "Practical application of building integrated photovoltaic (BIPV) system using transparent amorphous silicon thin-film PV module," *Sol. Energy*, vol. 85, no. 5, pp. 723–733, 2011.
- [33] L. Olivieri, E. Caamano-Martin, F. J. Moralejo-Vazquez, N. Martin-Chivelet, F. Olivieri, and F. J. Neila-Gonzalez, "Energy saving potential of semi-transparent photovoltaic elements for building integration," *Energy*, vol. 76, pp. 572–583, 2014.
- [34] K. Kapsis and A. K. Athienitis, "A study of the potential benefits of semi-transparent photovoltaics in commercial buildings," *Sol. Energy*, vol. 115, pp. 120–132, 2015.
- [35] L. Lu and K. M. Law, "Overall energy performance of semi-transparent single-glazed photovoltaic (PV) window for a typical office in Hong Kong," *Renew. Energy*, vol. 49, pp. 250–254, 2013.
- [36] L. Gaillard, C. Ménézo, S. Giroux, H. Pabiou, and R. Le-Berre, "Experimental Study of Thermal Response of PV Modules Integrated into Naturally-ventilated Double Skin Facades," *Energy Procedia*, vol. 48, pp. 1254–1261, 2014.
- [37] L. Gaillard, S. Giroux-Julien, C. Ménézo, and H. Pabiou, "Experimental evaluation of a naturally ventilated PV double-skin building envelope in real operating conditions," *Sol. Energy*, vol. 103, pp. 223–241, 2014.
- [38] J. Peng, D. C. Curcija, L. Lu, S. E. Selkowitz, H. Yang, and W. Zhang, "Numerical investigation of the energy saving potential of a semi-transparent photovoltaic double-skin facade in a cool-summer Mediterranean climate," *Appl. Energy*, vol. 165, pp. 345–356, 2016.
- [39] A. De Gracia, A. Castell, L. Navarro, E. Oró, and L. F. Cabeza, "Numerical modelling of ventilated facades: A review," *Renew. Sustain. Energy Rev.*, vol. 22, pp. 539–549, 2013.
- [40] J. M. Blanco, A. Buruaga, E. Rojí, J. Cuadrado, and B. Pelaz, "Energy assessment and optimization of perforated metal sheet double skin façades through Design Builder; A case study in Spain," *Energy Build.*, vol. 111, pp. 326–336, 2016.
- [41] L. Mei, D. Infield, U. Eicker, and V. Fux, "Thermal modelling of a building with an integrated ventilated PV facade," *Energy Build.*, vol. 35, no. 6, pp. 605–617, 2003.

- [42] A. S. Anđelković, I. Mujan, and S. Dakić, "Experimental validation of a EnergyPlus model: Application of a multi-storey naturally ventilated double skin façade," *Energy Build.*, vol. 118, pp. 27–36, 2016.
- [43] S. Flores Larsen, C. Filippin, and G. Lesino, "Modeling double skin green facades with traditional thermal simulation software," *Sol. Energy*, vol. 121, pp. 56–67, 2015.
- [44] H. Elarga, F. Goia, A. Zarrella, A. Dal Monte, and E. Benini, "Thermal and electrical performance of an integrated PV-PCM system in double skin façades: A numerical study," *Sol. Energy*, vol. 136, pp. 112–124, 2016.
- [45] Matlab, "Matworks," 2016. [Online]. Available: <http://www.mathworks.com/>.
- [46] A. Tzempelikos, A. K. Athienitis, and P. Karava, "Simulation of facade and envelope design options for a new institutional building," *Sol. Energy*, vol. 81, no. 9, pp. 1088–1103, 2007.
- [47] J. F. Kreider, P. S. Curtiss, and A. Rabl, *Heating and Cooling of Buildings: Design for Efficiency*, Second. New York: McGraw-Hill, 2002.
- [48] A. K. Athienitis, *Building Thermal Analysis*. 1993 Math Soft, Inc, 1998.
- [49] A. K. Athienitis and M. Stylianou, "Method and Global Relationship for Estimation of Transmitted Solar Energy Distribution in Passive Solar Rooms Method and Global Relationship for Estimation of Transmitted Solar Energy Distribution in Passive Solar Rooms," vol. 8312, no. August, 2016.
- [50] M. Sandberg, "Cooling of Building Integrated Photovoltaics by Ventilation Air," *IEA-ECB&CS Annex 35*, 1999.
- [51] S. Pantic, L. Candanedo, and a. K. Athienitis, "Modeling of energy performance of a house with three configurations of building-integrated photovoltaic/thermal systems," *Energy Build.*, vol. 42, no. 10, pp. 1779–1789, 2010.
- [52] G. N. Walton, *Algorithms for Calculating Radiation View Factors Between Plane Convex Polygons With Obstructions*. National Bureau of Standards, NBSIR 86-3463, 1986.
- [53] A. B. Shapiro, "Computer Implementation, Accuracy, and Timing of Radiation View Factor Algorithms," *ASME J. Heat Transf.*, no. 107, pp. 730–732, 1985.
- [54] F. P. . Incropera and D. P. DeWitt, *Introduction to Heat Transfer*, 6th editio. Wiley, 2011.
- [55] M. G. Emmel, M. O. Abadie, and N. Mendes, "New external convective heat transfer coefficient correlations for isolated low-rise buildings," *Energy Build.*, vol. 39, no. 3, pp. 335–342, 2007.
- [56] W. Lou, M. Huang, M. Zhang, and N. Lin, "Experimental and zonal modeling for wind pressures on double-skin facades of a tall building," *Energy Build.*, vol. 54, pp. 179–191, 2012.
- [57] M. Dongellini, C. Naldi, and G. L. Morini, "Sizing effects on the energy performance of reversible air-source heat pumps for office buildings," *Appl. Therm. Eng.*, vol. 114, pp. 1073–1081, 2017.
- [58] Z. Ioannidis, "Double Skin Facades Integrating Photovoltaic Panels , Motorized Shades and Controlled Air Flow," Concordia University, 2016.
- [59] L. Liao, "NUMERICAL AND EXPERIMENTAL INVESTIGATION OF BUILDING- INTEGRATED PHOTOVOLTAIC-THERMAL SYSTEMS," no. September, 2005.
- [60] C. F. Reinhart, J. A. Jakubiec, and D. Ibarra, "DEFINITION OF A REFERENCE OFFICE FOR STANDARDIZED EVALUATIONS OF DYNAMIC FAÇADE AND LIGHTING TECHNOLOGIES 1 Massachusetts Institute of

Technology , Cambridge , MA 02139 , USA 2 Harvard University , Graduate School of Design , Cambridge , MA 02138 , USA," *13th Conf. Int. Build. Perform. Simul. Assoc.*, pp. 3645–3652, 2013.

- [61] C. K. Wilkins and M. H. Hosni, "Plug load design factors," *ASHRAE J.*, vol. 53, no. 5, pp. 30–34, 2011.

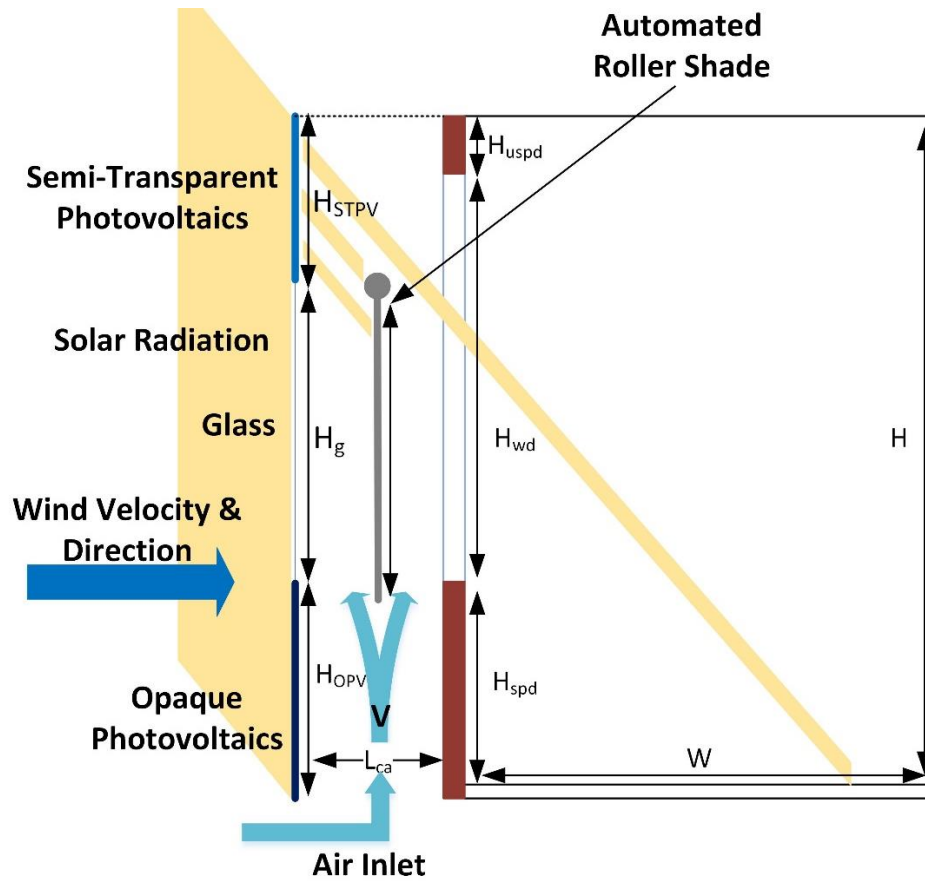


Figure 1. Sketch of the double façade section (one floor)

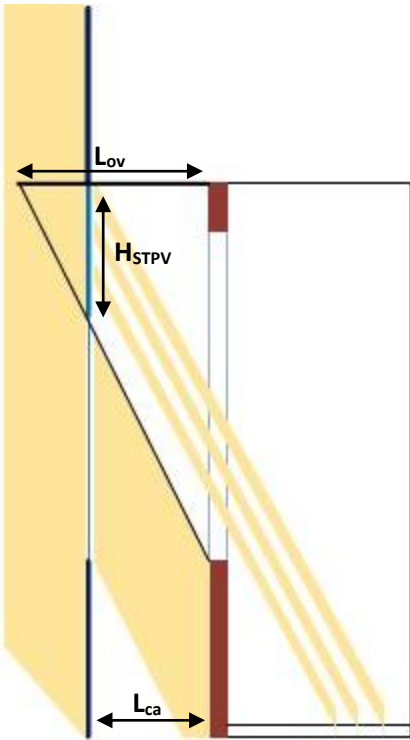


Figure 2. Photovoltaics act as overhangs

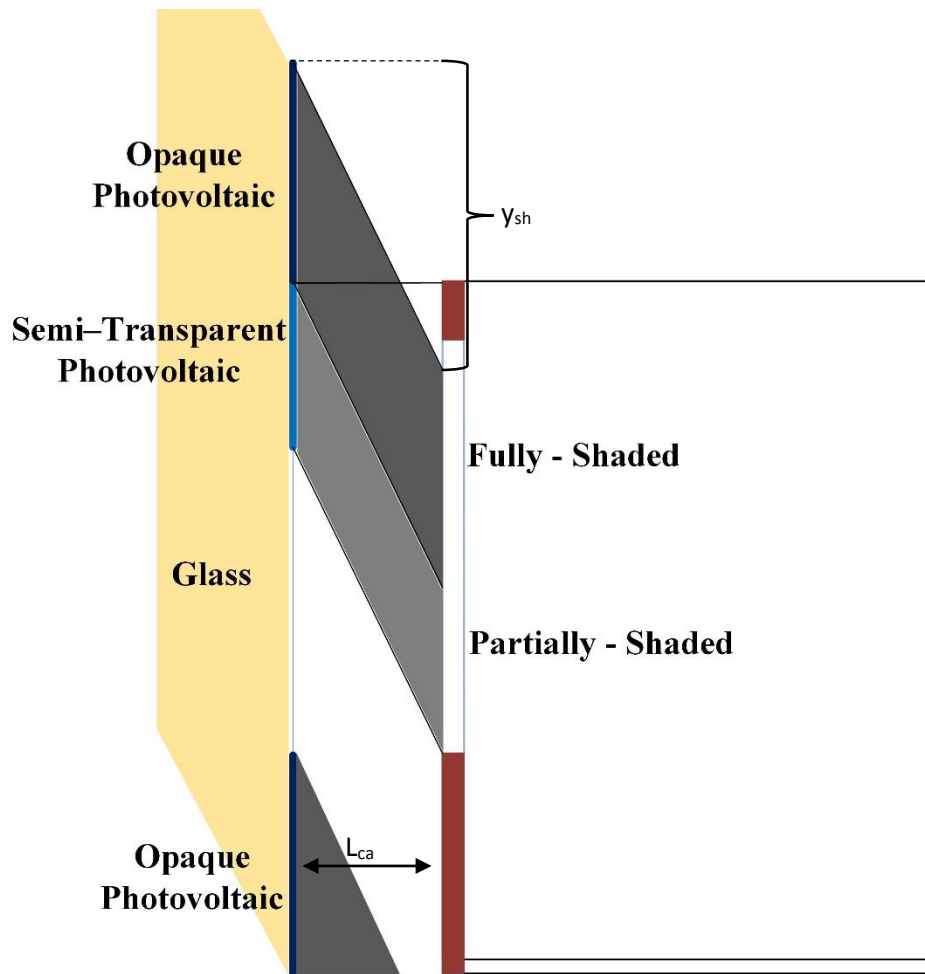


Figure 3. Shadows from the exterior skin to the interior. Fully shade from the opaque and partially-shade from the semi-transparent photovoltaic.

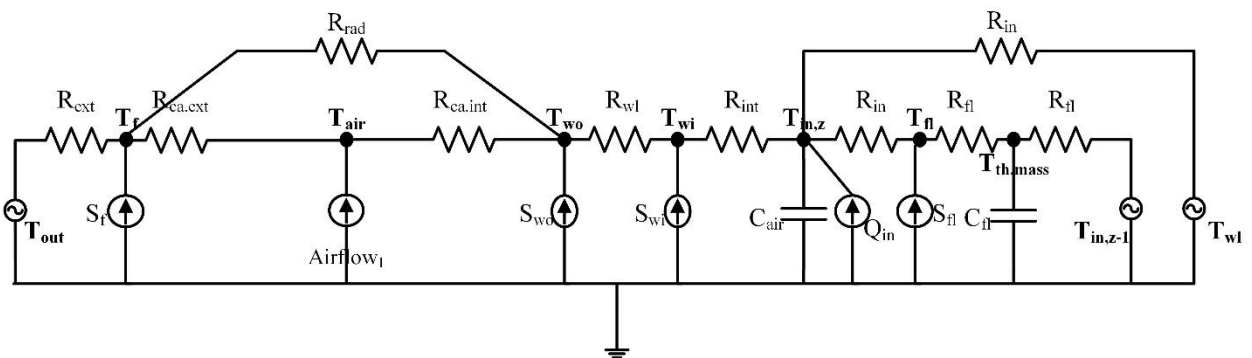


Figure 4. Thermal Network where there is no roller blind, having one airflow

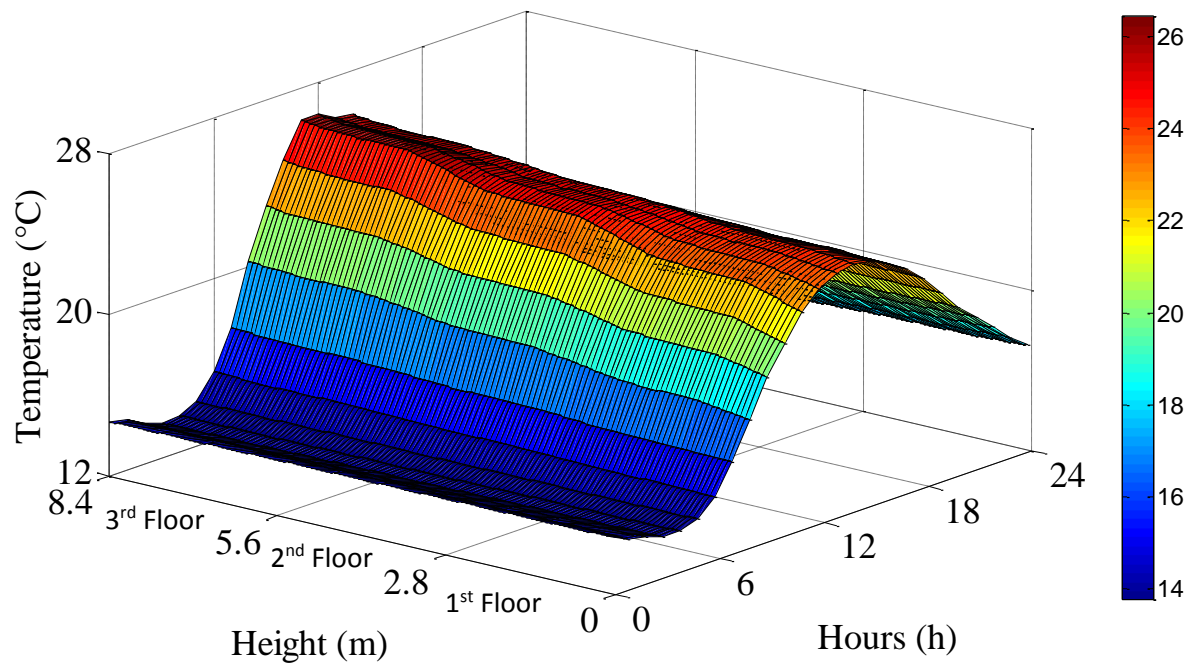


Figure 7. Air cavity temperature vs. the hours of the day and the façade height for a sample summer day (July 7th) and for $R_s = 0\%$ (no shading)

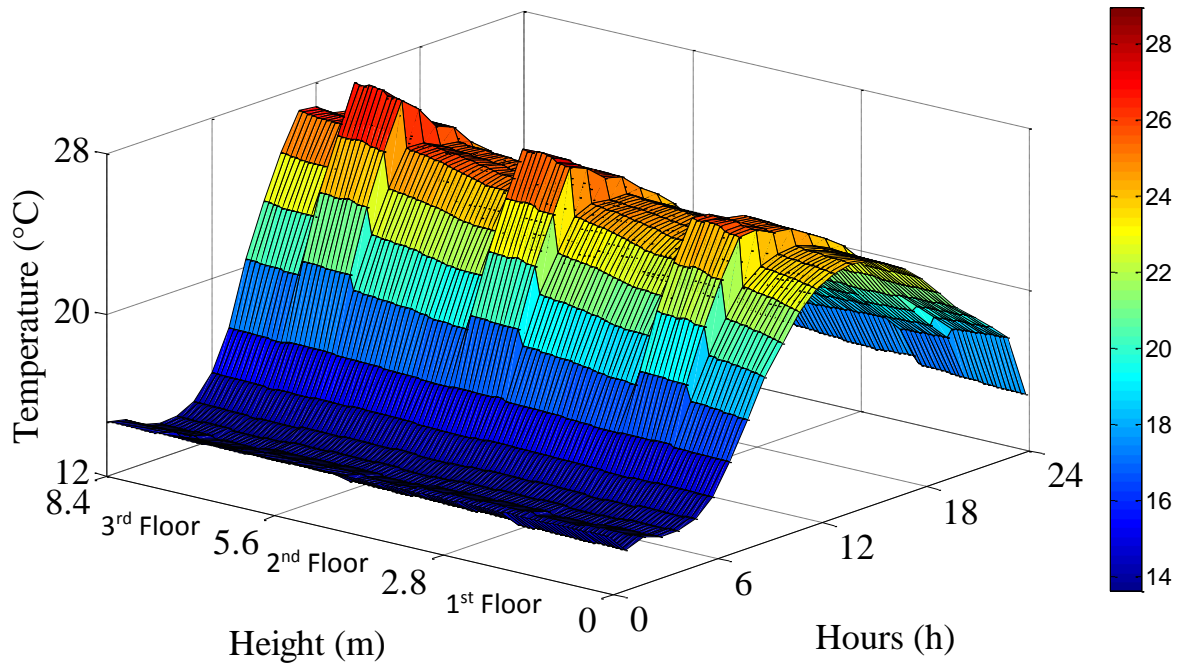


Figure 8. the hours of the day and the façade height for a sample summer day (July 7th) and for $R_s = 100\%$ (full shading)

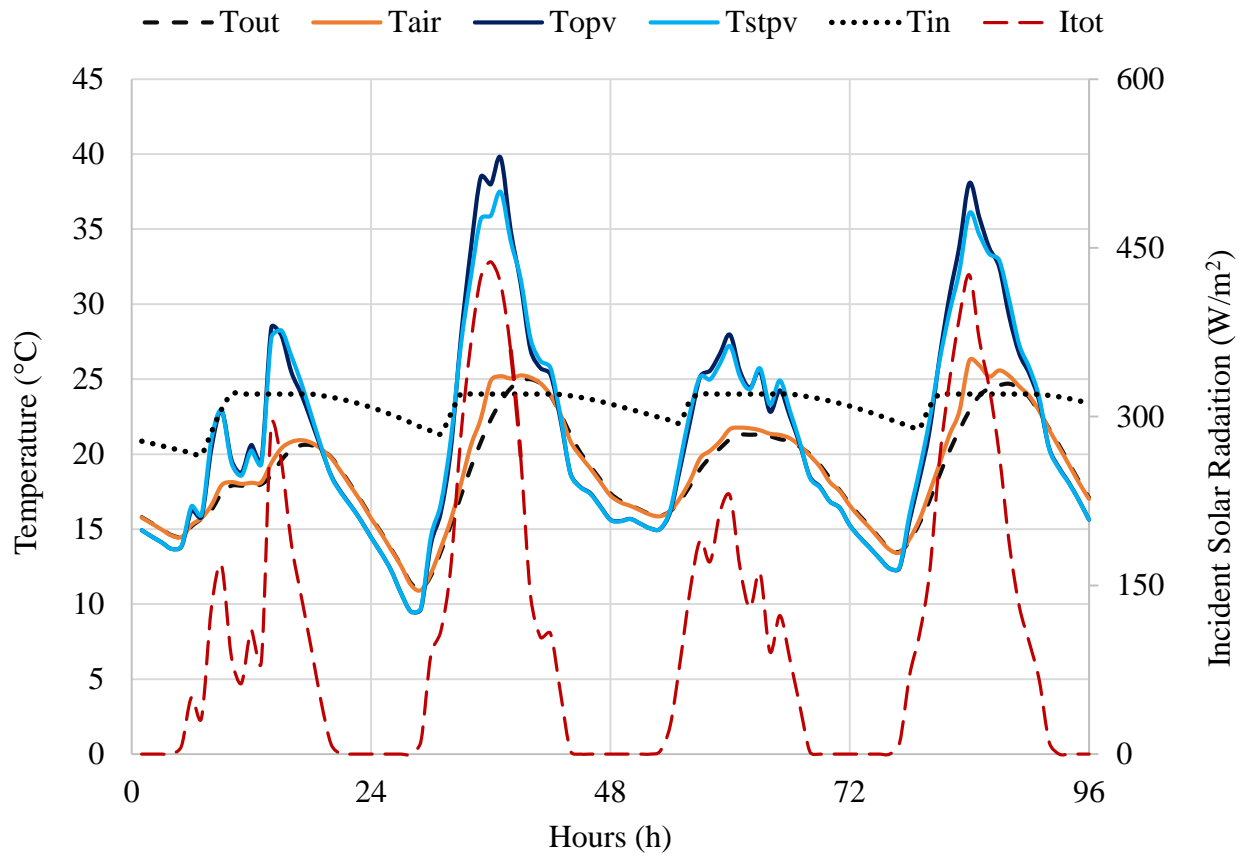


Figure 9. Time history of the OPV and STPV panels, ambient and cavity air and incident solar radiation for four sample summer days (June 29th - July 2nd)

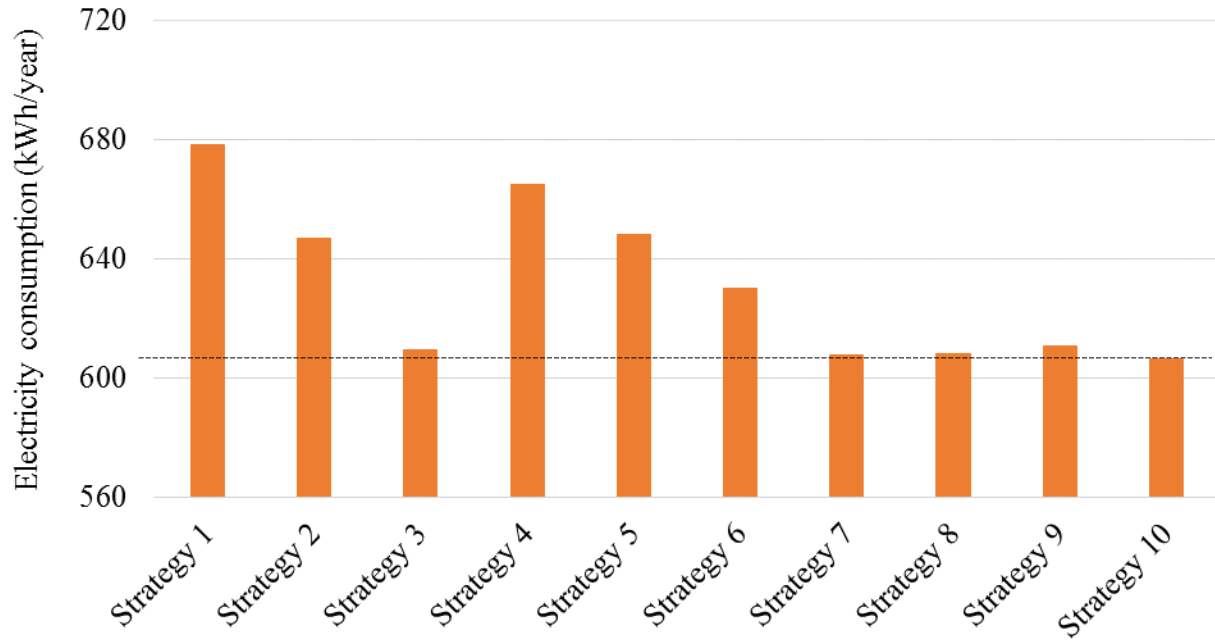


Figure 10. Building electricity consumption related to the airflow and fan operation strategies presented in Table 4

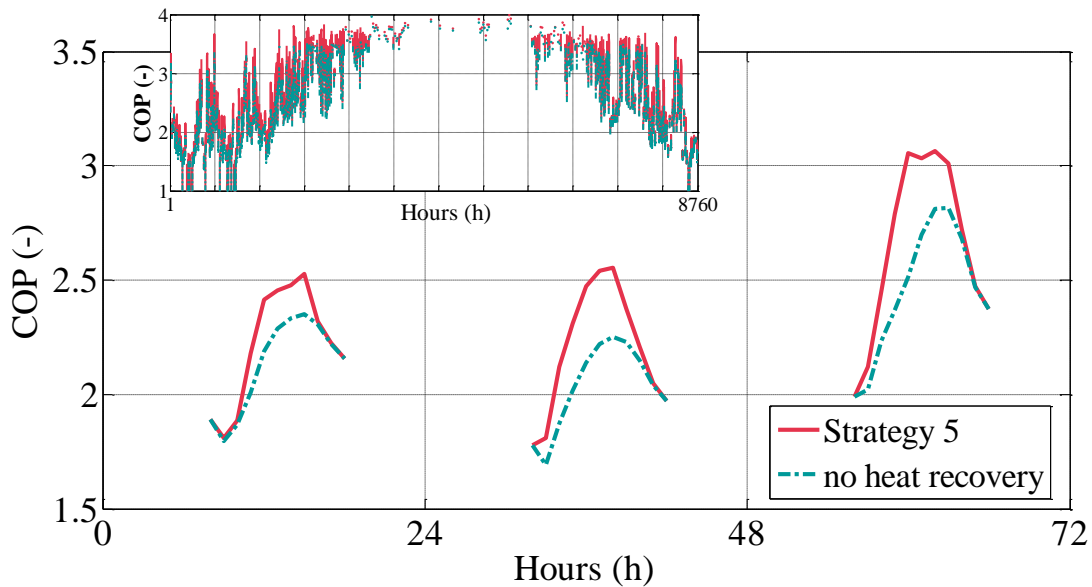


Figure 11. Hourly trend of heat pump COP for different heat recovery options, i.e. exhaust air modes (Strategy 5, Table 4) and outdoor air mode.

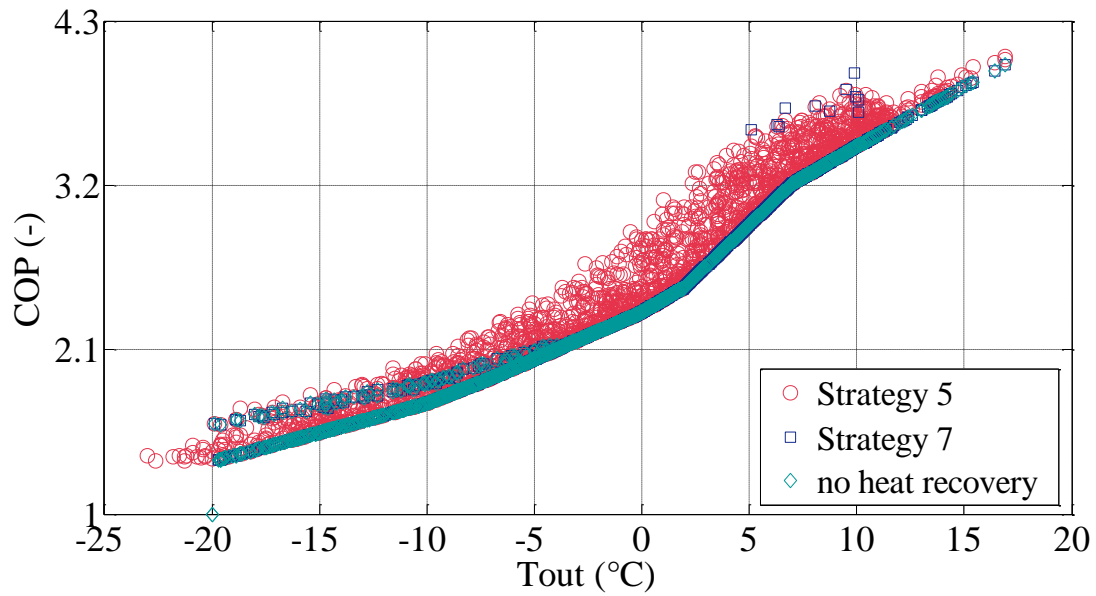


Figure 12. Heat pump COP vs. outdoor air temperature for different fan operation strategies

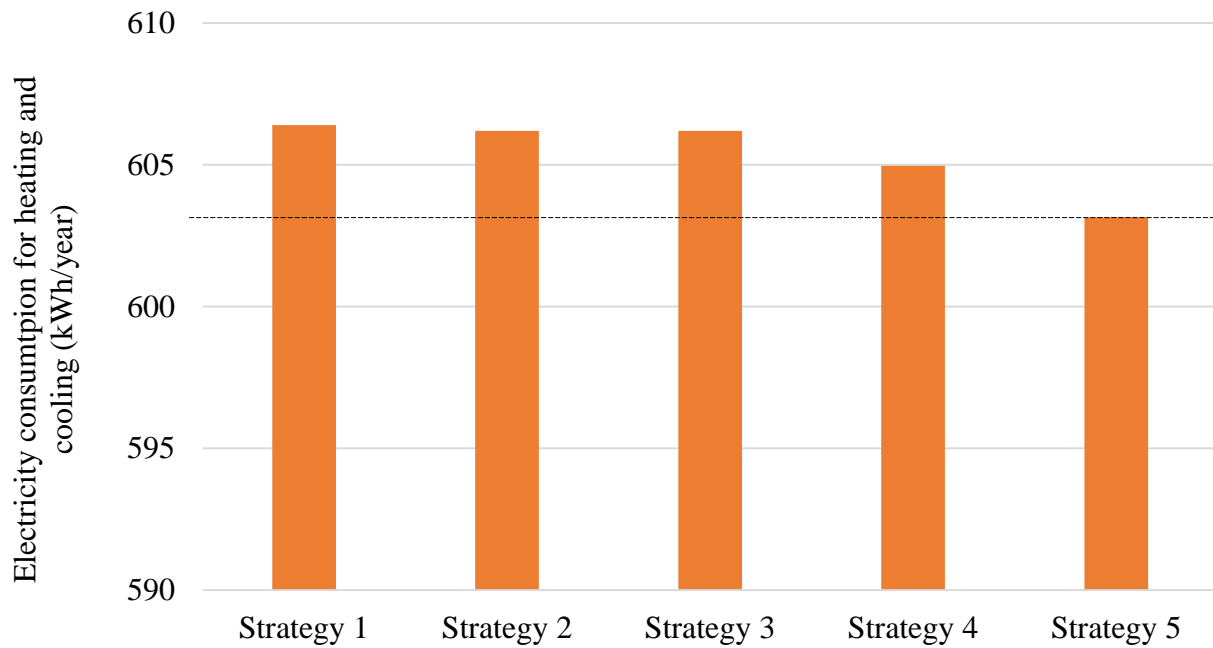


Figure 13. Building electricity consumption for heating and cooling for different roller blind control strategies

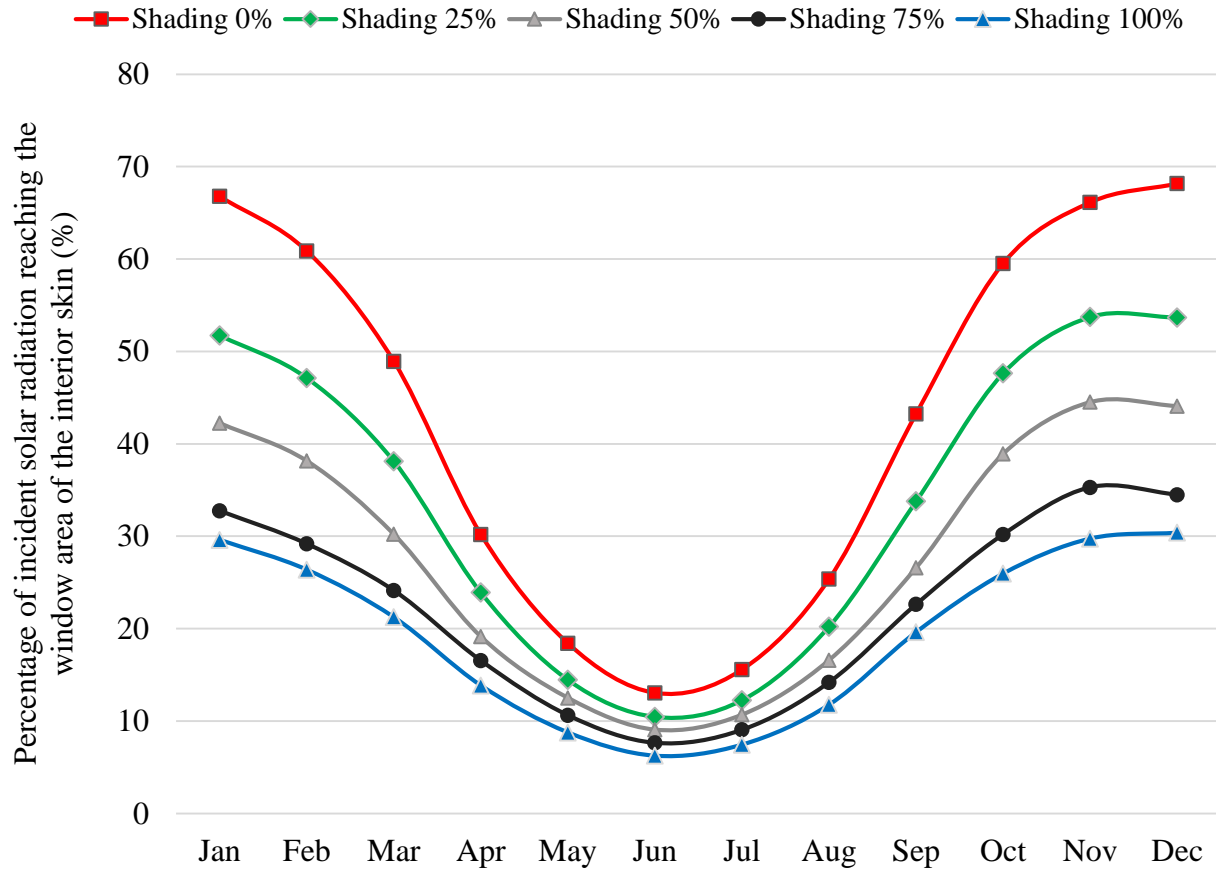


Figure 14. Percentage of the incident solar radiation reaching the window area at the interior surface of the double skin façade

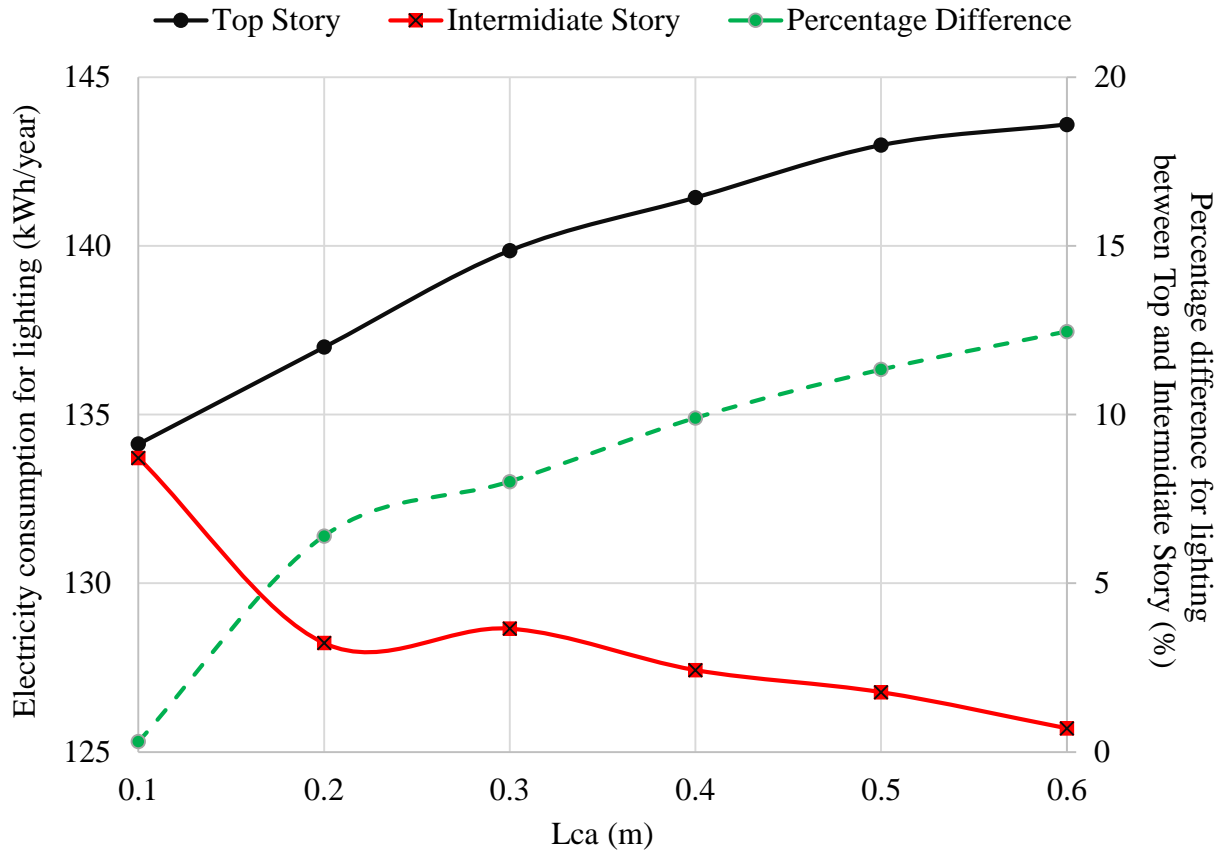


Figure 15. Electricity consumption of the building artificial lights as a function of the cavity thickness

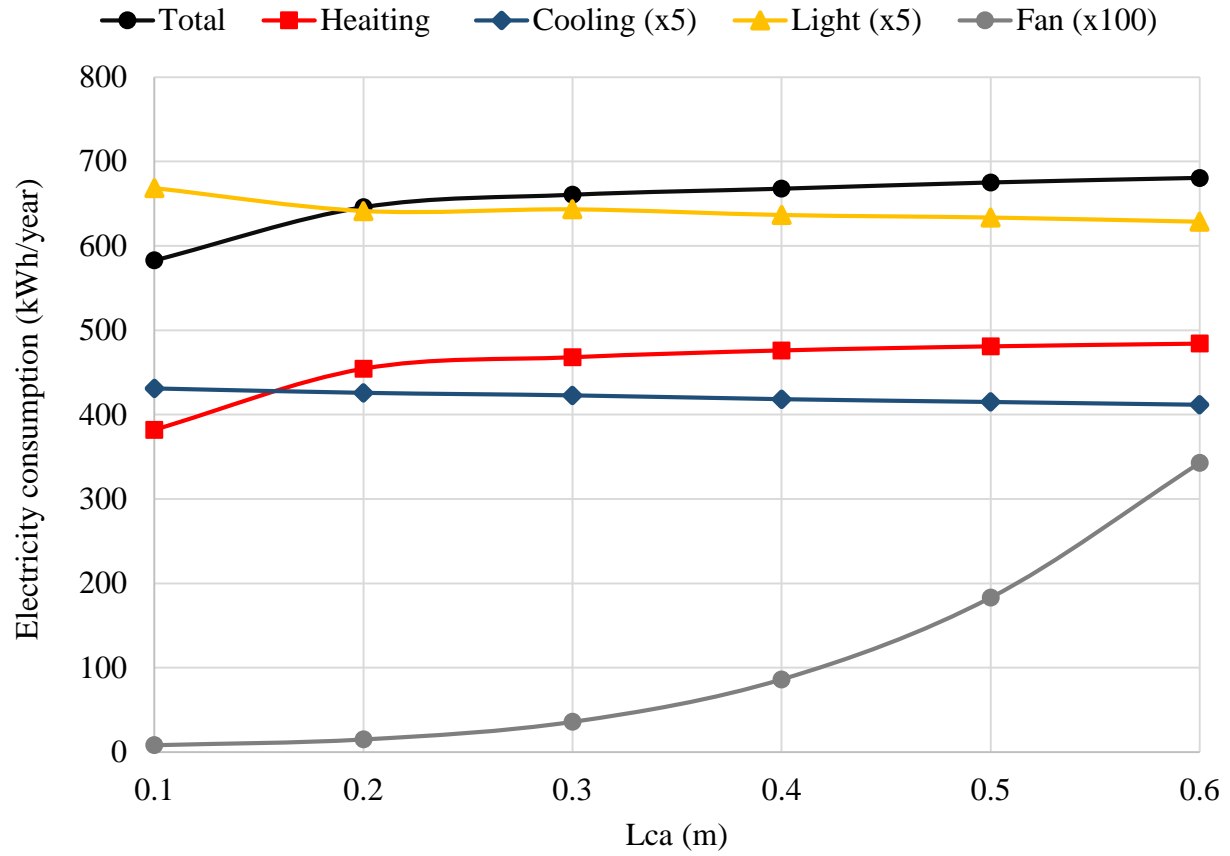


Figure 16. Yearly electricity consumption per floor required for heating, cooling, artificial lights and air cavity fans as a function of the air cavity thickness

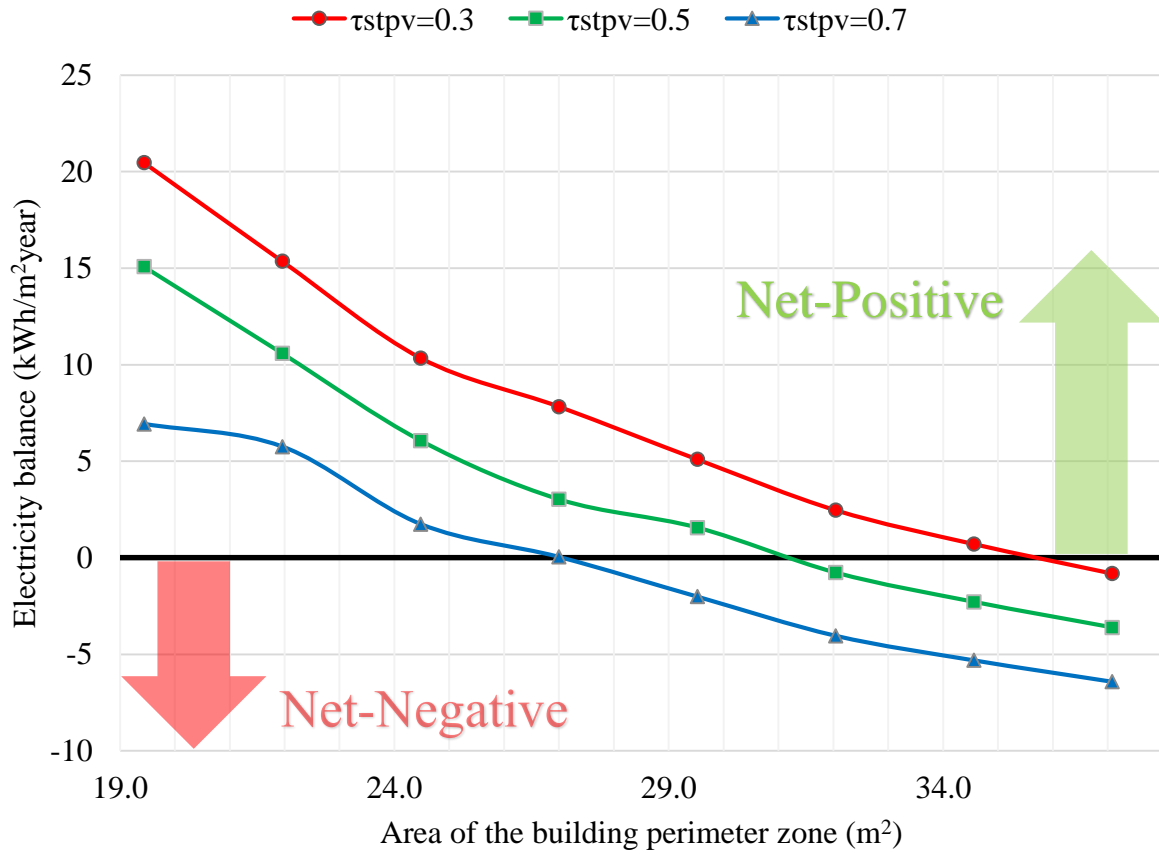


Figure 17. Electricity balance as a function of the semi-transparent PV panels transmittances and building perimeter zone area

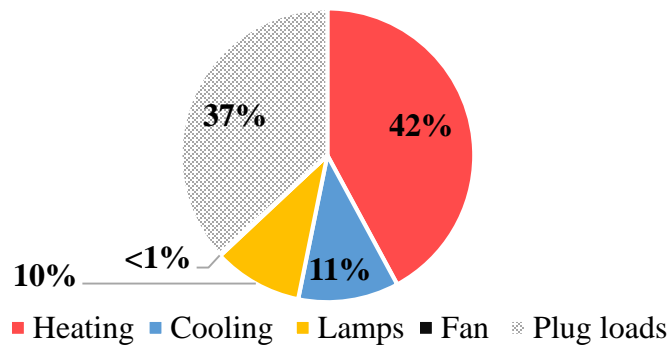


Figure 18. Percentage of the electricity consumption under Strategy 10 and $V_{sp} = 0.5$ m/s

Table 1. Input parameters of the numerical model

Design parameters	Number of floors		Optical properties	STPV transmittance
	Position of PV			Roller shade transmittance
	Position of roller blind			Glazing transmittance
	Interior skin design			PV efficiencies
Geometric parameters	H_{OPV}/H	H_{spd}/H	Thermal properties	Roller emissivity
	H_g/H	H_{wd}/H		Glazing emissivity
	H_{STPV}/H	H_{uspd}/H		SHCG
	L_{ca}/H	H_{rol}/H_g		Insulation of the room
	W	H		COP of the heat pump
Site properties	Location of the building		Flow properties	Reynolds number
	Orientation of the DSF-PV			Velocity
	PV			

Table 2. PV panel design parameters

Parameters	Value
Nominal power under STC	320 W
Temperature coefficient of PV efficiency β	0.5%
Reference temperature for PV efficiency	25°C
PV electrical efficiency at Tref	20%

Table 3. Comparison of experimental and predicted temperatures under quasi-state conditions

March 2004	T_{out} (°C)	Average velocity (m/s)	Incident solar radiation (W/m ²)	Measured		Simulated	
				T_{pv} (°C)	T_{ins} (°C)	T_{pv} (°C)	T_{ins} (°C)
10th	3.4	0.3	768.0	35.7	19.1	34.3	22.1

22th	-11.4	0.4	944.0	21.7	6.1	25.5	6.3
29th	9.7	0.4	714.0	34.5	23.6	35.5	22.8
30th	10.8	0.3	712.0	37.5	25.9	37.9	27.7

Table 4 Simulated strategies for the airflow and the fan operation

	Always	Day	Night	Tca > Troom	Tca < Troom	Heating mode	Cooling mode	Else
Strategy 1	MVent							
Strategy 2	NVent							
Strategy 3	Closed							
Strategy 4		MVent	NVent					
Strategy 5		MVent	Closed					
Strategy 6		NVent	Closed					
Strategy 7				MVent	Closed			
Strategy 8				NVent	Closed			
Strategy 9						Closed	MVent	NVent
Strategy 10						Closed	MVent	

Table 5. Simulated strategies for the control of the roller blind with shading (Rs = 100%) or without (Rs = 0%)

	Always	Heating mode	Cooling mode	Day and Tca > Troom	Day and Tca < Troom	Day and heating mode	Day and cooling mode	Else
Strategy 1	0%							
Strategy 2		0%	100%					
Strategy 3				100%	0%			0%
Strategy 4				100%	0%			100%
Strategy 5						0%	100%	100%

Table 6. Percentage frequency distribution (%) of COP occurrences calculated for the investigated fan operation strategies and no heat recovery modes.

COP intervals	HP							AH
	4.0–4.5	3.5–4.0	3.0–3.5	2.5–3.0	2.0–2.5	1.5–2.0	1.0–1.5	–
Strategy 1	0.2	12.7	21.9	14.9	27.2	20.8	2.3	0.0
Strategy 2	0.3	13.5	22.1	14.5	27.3	19.4	2.4	0.6
Strategy 4	0.2	12.7	21.9	14.9	27.2	20.9	2.3	0.0
Strategy 5	0.1	12.7	21.9	14.9	27.1	20.9	2.4	0.0
Strategy 7	0.0	3.9	21.8	14.5	29.4	23.8	2.8	3.7
Strategy 8	0.0	3.9	21.8	14.5	29.4	23.8	2.8	3.7
no heat recovery	0.0	3.4	22.2	14.5	29.4	23.8	2.8	3.7

Table 7. Electricity consumption of the building perimeter zone

	(kWh/year)
Heating	481.1
Cooling	126.7
Artificial lights	112.3
Fan	1.8
Plug loads	420.8
Total electricity consumption	1142.7